A negative imaginary robust formation control scheme for networked multi-tilt tricopters utilizing an inner-loop sliding-mode control technique ?

DOI:
10.1016/j.automatica.2024.111813

Document Version
Accepted author manuscript

A negative imaginary robust formation control scheme for networked multi-tilt tricopters utilizing an inner-loop sliding-mode control technique ⋆

Daniel Abara [a,c], Parijat Bhowmick [b], Alexander Lanzon [a]

[a] *Control Systems Centre, Department of EEE, School of Engineering, University of Manchester, Manchester M13 9PL, UK.*

[b] *Department of EEE and Centre for ICPS, Indian Institute of Technology Guwahati, Assam–781039, India.*

[c] *Department of EEE, University of Cross River State, Calabar, Nigeria.*

Abstract

This paper proposes a robust formation control scheme for networked multi-tilt tricopter UAVs utilizing the Negative Imaginary (NI) and Positive Real (PR) theory. A Sliding Mode Control (SMC) scheme is designed for a multi-tilt tricopter to ensure stable hovering at a desired height. Then, a modified Subspace-based system identification algorithm is devised to identify a six-by-six NI model of the inner-loop-SMC-controlled tricopter in the continuous-time domain by exploiting the Laguerre filter. A two-loop formation control scheme has been developed for networked multi-tilt tricopters where the inner loop of each tricopter applies the SMC scheme, and the outer loop implements a distributed output feedback controller that satisfies the 'mixed' Strictly NI (SNI) + Strictly PR (SPR) system properties. Subsequently, we have established the robustness of the proposed scheme against NI/PR-type uncertainties and sudden loss of agents. The eigenvalue loci (also known as characteristic loci) technique is used instead of the Lyapunov-based approach to prove the asymptotic stability of the formation control scheme. An in-depth simulation case study was performed on a group of six inner-loop-SMC-controlled multi-tilt tricopters connected via a network to achieve a formation control mission, even in the presence of uncertainties.

Key words: Negative Imaginary (NI) systems, Positive Real (PR) systems, multi-tilt tricopter, subspace-based system identification, formation control, characteristic loci, Sliding mode control, uncertainty, loss of agents.

1 Introduction

Cooperative control of multirotor Unmanned Aerial Vehicles (UAVs) has gained significant attention both from academia and industry due to the improved reliability and efficiency it offers, leading to a vast number of applications [25] including search and rescue [33], pipeline inspection and surveillance [35] among others. This attention has led to more efficient configurations and innovations in size, flight range, airframe configuration and other factors. The reader can refer to [27] for an exhaustive review of multirotor UAVs. An innovative platform with significant properties is a multi-tilt tricopter [13] with three rotors which can independently tilt, offering greater agility and flexibility. In contrast to the more common quadrotor [17] where trajectory tracking is achieved by manipulating the attitude, the multi-tilt tricopter considered in this work can achieve simultaneous independent attitude and trajectory tracking (complete 6-DOF control), due to its airframe configuration. In other words, it is possible to translate in the lateral and longitudinal directions without changing the attitude, thereby overcoming the limitation of quadrotors. This serves as our justification and motivation for investigating the cooperative control of the multi-tilt tri-

⋆ This work was supported by the Nigerian Petroleum Technology Development Fund (PTDF), the Engineering and Physical Sciences Research Council (EPSRC) [grant number EP/R008876/1] and by the Science and Engineering Research Board (SERB), DST, India [grant numbers SRG/2022/000892 and CRG/2022/006114]. All research data supporting this publication are directly available within this publication. For the purpose of open access, the authors have applied a Creative Commons Attribution (CC BY) licence to any Author Accepted Manuscript version arising. Corresponding author P. Bhowmick.

Email addresses: daniel.abara@manchester.ac.uk (Daniel Abara), parijat.bhowmick@iitg.ac.in (Parijat Bhowmick), Alexander.Lanzon@manchester.ac.uk (Alexander Lanzon).

copter rather than the quadcopter, thus creating more possibilities when performing specialised and more complex tasks. One of the most investigated coordination problems of multi-agent systems (MASs) is the formation control problem, with the key concern being the development of control strategies to achieve group formation control. Several approaches [10], [40], [42] have been proposed to solve the formation control problem, including the more recent Negative Imaginary (NI) approach [44, 36, 38, 12]. NI theory was initially inspired by the 'positive position feedback control' of highly resonant systems [18]. It initially drew attention as a control technique for vibration control of flexible structures [3, 45, 20], large space structures and robotic manipulators [23], and later saw applications in nano-positioning [28], vehicle platooning [5], train platooning [19] and cooperative control of two-wheeled mobile robots [36]. The critical feature driving this growth is its simple internal stability condition that is, a necessary and sufficient condition for the internal stability of a positive feedback interconnection of NI and SNI systems $M(s)$ and $N(s)$, is $\lambda_{\max}[N(0)M(0)] < 1$ [18], [16], which is a condition that depends on the loop gain at zero frequency only. NI theory has been utilised in [38] and [39] to design a consensus-based formation control framework for a multi-vehicle system together with an obstacle detection and avoidance algorithm. They have utilised the results of [44] and [43] to develop a particular consensus and formation control framework for heterogeneous autonomous vehicles facilitating time-invariant switching.

Motivated by the results above and applications and to improve the formation control of multi-agent UAVs, this paper develops a leader-following formation control scheme for a network of multi-tricopter systems. The idea of utilising the NI-SNI closed-loop stability result to develop a cooperative control scheme for the tricopter stems from the fact that a particular class of UAV systems can be modelled as a group of networked single/double integrator agents (typically by feedback linearisation), which inherently satisfies the NI property with poles at the origin. It has also been shown in [38] and [39] that linearized dynamics of the inner-loop of a class of UAVs (closed-loop dynamics) exhibit the negative imaginary property. Consequently, a cooperative control scheme can be deployed as the outer-loop controller. The main contributions of this paper are as follows: (1) We derive the nonlinear model of a multi-tilt tricopter using force and torque kinematics and dynamics too. Although the feedback linearization technique yields single or double integrator systems, as previously mentioned, it lacks the accuracy of the system model as it relies on the nonlinearity-cancellation by introducing an inverse nonlinear function. Hence, we use sliding mode control laws to linearize the inner loop of the multi-tilt tricopter UAV without sacrificing much of its original properties and, at the same time, stabilising the system. Thus, we obtain an SMC-controlled closed-loop system with six inputs and outputs corresponding to the tricopter's Cartesian positions and attitude. (2) To characterize the inner-loop-SMC-controlled as an NI system, we develop a closed-loop system identification algorithm that guarantees that the resultant model is NI. The algorithm exploits the classic subspace method but in continuous time by use of the Laguerre filter [8] in the identification process, and its advantages and simplicity are highlighted. (3) The proposed identification algorithm is then applied to find NI models for all six channels of the inner-loop-SMC-controlled multi-tilt tricopter. The frequency responses of the identified models are used to verify whether the models exhibit the NI property. (4) A closed-loop stability result is developed for networked NI/SNI systems using a 'mixed' Strictly Negative Imaginary (SNI) plus Strictly Positive Real (SPR) controller in a negative feedback interconnection. (5) An 'output feedback distributed SNI+SPR control' law is proposed for achieving robust cooperative control combining leader-following consensus and formation control principles. Rather than the Lyapunov method, we use a new method to prove the convergence of the control problem, which encompasses formation control and cooperative tracking, exploiting the characteristics of the characteristic loci of networked NI and SNI systems. The term 'mixed' with respect to the NI+SPR controller implies that for some of the channels of the tricopter, the controller is SNI, while for others, the controller is SPR. (6) Finally, a simulation case study involving a group of six inner-loop-SMC-controlled multi-tilt tricopter agents is provided to demonstrate the usefulness and effectiveness of the proposed scheme.

Notation: $\mathbb{R}_{\geq 0}$ and $\mathbb{R}_{>0}$ denote respectively the sets of all non-negative and all positive real numbers. $I_n \in \mathbb{R}^{n\times n}$ denotes the identity matrix of dimension $n \times n$, $\text{diag}\{a, b, c\}$ represents a diagonal matrix with diagonal entries a, b, c. $\mathbf{a}^e$, $\mathbf{a}^b$ and $\mathbf{a}^{l^n}$ denote a vector $\mathbf{a}$ given relative to the earth (inertial), body and local frame n respectively. $\mathscr{R}^{m\times n}$ denotes the set of all proper, real, rational transfer function matrices, and $\mathscr{RH}_\infty^{m\times n}$ denotes the set of all proper, real, rational and asymptotically stable transfer function matrices, both of dimensions $(m\times n)$. For a transfer function matrix $M(s)$, $M(j\omega)^* = M(-j\omega)^\top$ and $M(s)^* = M(\bar{s})^\top$ where $\bar{s}$ denotes the complex conjugate of s. The frequency response real-Hermitian and imaginary-Hermitian parts of $M(s)$ are given by $\frac{1}{2}[M(j\omega) + M(j\omega)^*]$ and $\frac{1}{2j}[M(j\omega) - M(j\omega)^*]$ respectively. $A \otimes B$ indicates the Kronecker product of two matrices A and B.

2 Preliminaries and problem formulation

This section serves the purpose of building a solid technical background for developing the main results of this paper and reveals the problem statement. The frequently-used terminologies related to coordinate rotations, algebraic graph theory, basics of NI and PR systems theory,

and the concept of multi-agent NI systems have been provided.

2.1 Coordinate rotations

The transformation of a vector from the inertial to body frame following the (z, y, x) Euler rotation sequence [37] is encoded in the rotation matrix

$$\boldsymbol{R}_e^b(\boldsymbol{\eta}) = \begin{bmatrix} c_\theta c_\psi & c_\theta s_\psi & -s_\theta \\ s_\phi s_\theta c_\psi - c_\phi s_\psi & s_\phi s_\theta s_\psi + c_\phi c_\psi & s_\phi c_\theta \\ c_\phi s_\theta c_\psi + s_\phi s_\psi & c_\phi s_\theta s_\psi - s_\phi c_\psi & c_\phi c_\theta \end{bmatrix}, \quad (1)$$

where $\boldsymbol{\eta} = [\phi \ \ \theta \ \ \psi]^\top$, $c_\phi \triangleq \cos\phi$ and $s_\phi \triangleq \sin\phi$. The reverse transformation is the inverse $\boldsymbol{R}_e^b(\boldsymbol{\eta})^{-1} = \boldsymbol{R}_e^b(\boldsymbol{\eta})^\top = \boldsymbol{R}_b^e(\boldsymbol{\eta})$ from rotation matrix properties [37]. Similarly, the function which transforms the Euler angle rates from body to inertial frame is given in [37] as,

$$\boldsymbol{\Gamma} = \begin{bmatrix} 1 & \sin\phi\tan\theta & \cos\phi\tan\theta \\ 0 & \cos\phi & -\sin\phi \\ 0 & \sin\phi\sec\theta & \cos\phi\sec\theta \end{bmatrix}. \quad (2)$$

2.2 Algebraic graph theory

Consider a weighted and undirected graph $\mathscr{G} = (\mathscr{V}, \mathscr{E}, \mathscr{A})$ with a non-empty set of nodes $\mathscr{V} = \{1, 2, \cdots, N\}$, a set of edges $\mathscr{E} \subset \mathscr{V} \times \mathscr{V}$ and the associated adjacency matrix $\mathscr{A} = [a_{ij}] \in \mathbb{R}^{N\times N}$. An edge rooted at the i^{th} node and ended at the j^{th} node is denoted by (i, j), which means information can flow from the i^{th} node to the j^{th} node. a_{ij} is the weight of edge (j, i) and $a_{ij} > 0$ if $(j, i) \in \mathscr{E}$. The j^{th} node is called a neighbour of the i^{th} node if $(j, i) \in \mathscr{E}$. The in-degree matrix is defined as $\mathscr{D} = \text{diag}\{d_i\} \in \mathbb{R}^{N\times N}$ with $d_i = \sum_{j=1}^N a_{ij}$. The Laplacian matrix $\mathscr{L} \in \mathbb{R}^{N\times N}$ of $\mathscr{G}$ is defined as $\mathscr{L} = \mathscr{D} - \mathscr{A}$. If the i^{th} agent is connected to the leader (considered as the target or root node labelled with '0'), an edge $(0, i)$ is said to exist between them with a pinning gain $g_i > 0$.

2.3 Negative Imaginary and Positive Real theory

We will now recall the definitions of NI and SNI systems.

Definition 1 ***(NI System)*** *[23, 16] Let $M(s)$ be the real, rational and proper transfer function matrix of a finite-dimensional and square system M with no RHP poles. Then, $M(s)$ is said to be NI if*

- *$j[M(j\omega) - M(j\omega)^*] \geq 0 \ \forall\omega \in (0, \infty)$ except the values of ω where $s = j\omega$ is a pole of $M(s)$;*
- *If $s = j\omega_0$ with $\omega_0 \in (0, \infty)$ is a pole of $M(s)$, then it is at most a simple pole and the residue matrix $\lim_{s\to j\omega_0}(s - j\omega_0)jM(s)$ is Hermitian and positive semidefinite;*
- *If $s = 0$ is a pole of $M(s)$, then $\lim_{s\to 0} s^k M(s) = 0 \ \forall k \geq 3$ and $\lim_{s\to 0} s^2 M(s)$ is Hermitian and positive semidefinite.*

Definition 2 ***(SNI System)*** *[18, 16] Let $M(s)$ be the real, rational and proper transfer function matrix of a finite-dimensional, square and causal system. Then, $M(s)$ is said to be SNI if $M(s)$ has no poles in $\{s \in \mathbb{C} : \Re[s] \geq 0\}$ and $j[M(j\omega) - M(j\omega)^*] > 0 \ \forall\omega \in (0, \infty)$.*

Below, we present the state-space characterization (NI lemma) of the class of NI systems without poles at the origin.

Lemma 1 ***(NI lemma)*** *[23, 16] Let (A, B, C, D) be a minimal state-space realization of a real, rational proper transfer function matrix $M(s)$ with no poles in $\{s \in \mathbb{C} : \Re[s] > 0\}$. Then, $M(s)$ is NI without any pole at the origin if and only if $\det[A] \neq 0$, $D = D^\top$ and there exists a real matrix $P = P^\top > 0$ such that*

$$AP + PA^\top \leq 0 \quad \text{and} \quad B + APC^\top = 0. \quad (3)$$

We will now recall the definition of Strictly Positive Real (SPR) systems.

Definition 3 ***(SPR system)*** *Let G be a finite-dimensional, square, LTI system with $G(s) \in \mathscr{RH}_\infty^{m\times m}$. Let $[G(s) + G^\sim(s)]$ have full normal rank m. Then, $G(s)$ is said to be an SPR system if*

$$G(j\omega) + G(j\omega)^* > 0 \qquad \forall\omega \in \mathbb{R}. \quad (4)$$

Ultimately, we would like to propose a new class of LTI systems that exhibits a 'mixed' SNI and SPR property. Originally, [30] proposed the notion of 'mixed' NI+Finite-gain system property and later, [7] defined a class of 'mixed' NI+Finite-gain+Passive systems along the direction of [30]. According to [30] and [7], a system is called 'mixed' SNI+SPR if it exhibits SNI property in some frequency intervals and SPR property in others. For example, $G_1(s) = \frac{(s+1)}{(s+6)(s^2+4s+8)}$, $G_2(s) = \frac{s+1}{(s^2+8s+32)}$, $G_3(s) = \frac{s+1}{(s+10)^3}$, etc. However, this 'mixed' property can be defined in another sense. A decoupled multivariable system with a diagonal transfer function matrix can be designated as a 'mixed' SNI+SPR system if it comprises a *mixture* of SNI and SPR transfer function elements, e.g., $G_4(s) = \text{diag}\{\frac{1}{s+1}, \frac{1}{s^2+s+1}, \frac{s+2}{s^2+8s+20}\}$. In this paper, we have designed a 'dynamic output feedback formation

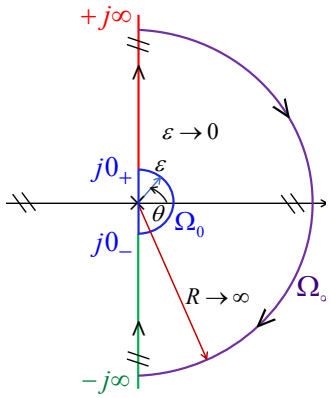

Fig. 1. Nyquist $\mathscr{D}$-contour in the s-plane.

control scheme' utilising this 'mixed' SNI+SPR system property (refer to Section 5 and Section 7).

Definition 4 *('Mixed' SNI+SPR property) Let G be a square, LTI system with a diagonal transfer function matrix $G(s) = \text{diag}\{g_1(s), g_2(s), \cdots, g_m(s)\}$. Let k be a positive integer and $0 < k < m$. Then, the system G is said to have 'mixed' SNI+SPR property if k number of constituent transfer function elements are SNI and the remaining $(m - r)$ number of elements are SPR.*

2.4 Characteristic loci theory

Similar to a Nyquist plot, the characteristic loci $\rho_i(s)$ for $i \in \{1, 2, \ldots, n\}$ of a transfer function matrix $G(s)$ is a conformal mapping of the function $\det[G(s)]$ in a complex plane, known as the characteristic loci plane, when s traverses along the s-plane $\mathscr{D}$-contour in the clockwise direction as shown in Fig. 1. For complete details of the characteristic loci theory, please see [2] and [24].

Theorem 1 *[2], [24] The negative feedback interconnection of a plant $M(s)$ and a controller $K(s)$ is asymptotically stable if and only if the net sum of the critical point $(-1 + j0)$ encirclements of all the characteristic loci $\rho_i(jw)$ of the loop transfer function $M(s)K(s)$ for $i \in \{1, 2, \ldots, n\}$ is counter-clockwise and equal to the number of RHP zeros of the open-loop characteristic polynomial.*

2.5 Multi-agent NI and SNI systems

This paper exploits multi-agent NI (also called distributed NI property) theory to develop a new cooperative control methodology for a group of networked (via an undirected graph) inner-loop-SMC-controlled (refer to Section 3) multi-tilt tricopters that exhibit the distributed NI property.

Assumption 1 *The communication topology of N homogeneous agents is described by an undirected and connected graph $\mathscr{G}$. A root node (leader or target) always exists that sends a reference trajectory to the follower agent(s).*

We will now review some fundamental properties of multi-agent NI systems. [44] first established that a homogeneous network of NI (or SNI) agents that satisfies Assumption 1, given by $\bar{M}(s) = (\mathscr{L} + \mathbb{G}) \otimes M(s)$, retains the NI (or SNI) property and $\bar{M}(0) > 0$ (or < 0) $\Leftrightarrow M(0) > 0$ (or < 0). Recently, [12] has derived an important property of a multi-agent NI system exploiting the results of [4]. It shows that all the characteristic loci $\lambda_i(j\omega)$ of a homogeneous multi-agent NI (or SNI) system lie in the union of the third and fourth quadrants of the complex plane (also known as the characteristic loci plane, discussed in Subsection 2.4). The following mathematical notation will be adopted: the phase angle contribution of each of the characteristic loci, denoted by $\phi_i(\lambda_i(j\omega))$, lies in the range $[-\pi, 0]$ $\forall \omega \geq 0$ (for *NI* systems) and respectively in the range $(-\pi, 0)$ $\forall \omega \in (0, \infty)$ (for *SNI* systems). This resembles the Nyquist interpretation of SISO NI and SNI transfer functions.

2.6 Problem formulation

Given a multi-agent system (e.g. a multi-UAV system) with N agents connected via a communication graph $\mathscr{G}$ that satisfies Assumption 1 and modelled as a group of networked agents with identical dynamics, the control problem is to design a two-loop distributed formation control scheme (Fig. 9) such that all agents converge to the state trajectory of the leader node and the agents asymptotically reach the desired static formation. That is, $\lim_{t \to \infty} (x_i(t) - x_0(t)) = 0$, $\forall i \in \{1, 2, \ldots, N\}$, where x_0 is the state of the leader node and x_i is the state of each individual agent.

3 Multi-tilt tricopter modelling

This section presents the model of the tricopter UAV under consideration. Note that a similar model is proposed in [13], [11]. The model linearization using the sliding mode control technique in closed-loop is also discussed.

3.1 Forces and moments

The multi-tilt tricopter as depicted in Fig. 2 is considered to be a rigid-body with mass m and centre of mass $\boldsymbol{G}$ where (X^e, Y^e, Z^e) denotes the earth (inertial) frame and (X^b, Y^b, Z^b) denotes the body frame with its origin at $\boldsymbol{G}$. The total force acting on the UAV $\mathbf{F}_t^b \in \mathbb{R}^3$ is the sum of the force produced by the rotors $\mathbf{F}_m^b$ and the force due to gravity $\mathbf{F}_g^e = [0\ 0\ mg]^\top$, where g is the gravity constant. The forces and drag torques produced by each rotor are assumed to be proportional to the square of the angular speeds ω_i [32] such that $f_i = k_t \omega_i^2$ and $\tau_i = k_d \omega_i^2, i \in \{1, 2, 3\}$ where f_i, τ_i denote the forces and drag

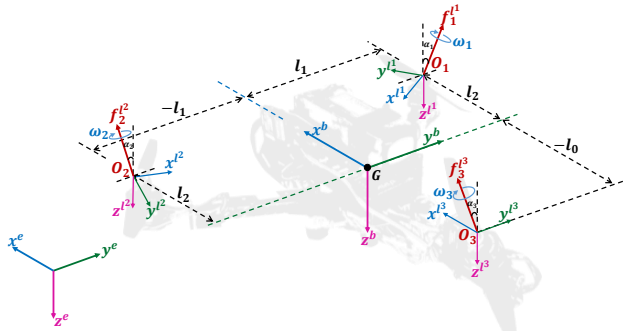

Fig. 2. The coordinate systems associated with a multi-tilt tricopter and the forces and torques acting on it.

torques respectively, and k_t, k_d denote the thrust and drag torque constants respectively. From Fig. 2, the 3D force produced by the i^{th} rotor in its local frame is given as $\boldsymbol{f}_i^{l^i} = [0 \;\; -k_t\omega_i^2 \sin\alpha_i \;\; -k_t\omega_i^2 \cos\alpha_i]^\top, i \in \{1,2,3\}$. The body frame forces for each rotor $\boldsymbol{f}_i^b$ are obtained by pre-multiplying the local frame forces $\boldsymbol{f}_i^{l^i}$ with (1) noting that first and second rotors need to be rotated 120^0 clockwise ($\psi = 2\pi/3$) and 120^0 counter-clockwise ($\psi = -2\pi/3$) respectively, both about the yaw axis, to align the local frames with the body frame. Note that $\boldsymbol{f}_3^{l^3} = \boldsymbol{f}_3^b$ as the third rotor is already aligned to the body frame. Thus, the total force from the three rotors in body coordinates is given by $\mathbf{F}_m^b = \sum_{i=1}^3 \boldsymbol{f}_i^b = k_t\boldsymbol{\Psi}_t\boldsymbol{\Omega}$ where $\boldsymbol{\Omega} = [\omega_1^2 s_{\alpha_1} \; \omega_2^2 s_{\alpha_2} \; \omega_3^2 s_{\alpha_3} \; \omega_1^2 c_{\alpha_1} \; \omega_2^2 c_{\alpha_2} \; \omega_3^2 c_{\alpha_3}]^{\mathrm{T}}$ and

$$\boldsymbol{\Psi}_t = \begin{bmatrix} -\frac{\sqrt{3}}{2} & \frac{\sqrt{3}}{2} & 0 & 0 & 0 & 0 \\ \frac{1}{2} & \frac{1}{2} & -1 & 0 & 0 & 0 \\ 0 & 0 & 0 & -1 & -1 & -1 \end{bmatrix}. \tag{5}$$

Using Fig. 2, let $\boldsymbol{G}_{o_i} = \begin{bmatrix} G_{o_{ix}} & G_{o_{iy}} & G_{o_{iz}} \end{bmatrix}^\top$ be the vector of the i^{th} rotor's distance from the centre of mass and (O_1, O_2, O_3) be the application points of $\boldsymbol{f}_1, \boldsymbol{f}_2, \boldsymbol{f}_3$ respectively, with $l_1 = \frac{\sqrt{3}}{2}l_0$ and $l_2 = \frac{1}{2}l_0$ where l_0 is the arm length. Then, the total moments from the rotors in the body frame is $\mathbf{T}_r^b = \sum_{i=1}^3 (\boldsymbol{G}_{o_i} \times \boldsymbol{f}_i^b) = k_t\boldsymbol{\Psi}_d\boldsymbol{\Omega}$ where

$$\boldsymbol{\Psi}_d = \begin{bmatrix} 0 & 0 & 0 & -l_1 & l_1 & 0 \\ 0 & 0 & 0 & l_2 & l_2 & -l_0 \\ l_0 & l_0 & l_0 & 0 & 0 & 0 \end{bmatrix}. \tag{6}$$

The drag torque of each rotor acts opposite to the i^{th} rotor's spin direction and is expressed as $\boldsymbol{\tau}_{d,i}^{l^i} = [0 \;\; -k_d\omega_i^2 \sin\alpha_i \;\; -k_d\omega_i^2 \cos\alpha_i]^\top \; \forall i \in \{1,2,3\}$ and in body frame as $\boldsymbol{\tau}_{d,i}^b$ obtained by pre-multiplying the local frame forces $\boldsymbol{\tau}_{d,i}^{l^i}$ with (1) like the case of rotor forces such that the total moments due to drag from the three rotors is $\mathbf{T}_d^b = \sum_{i=1}^3 \boldsymbol{\tau}_{d,i}^b = k_d\boldsymbol{\Psi}_t\boldsymbol{\Omega} \; \forall i \in \{1,2,3\}$. Consequently, the total moments acting on the tricopter is $\mathbf{T}_m^b = \mathbf{T}_r^b + \mathbf{T}_d^b = (k_t\boldsymbol{\Psi}_d + k_d\boldsymbol{\Psi}_t)\boldsymbol{\Omega} \in \mathbb{R}^3$. By vertically stacking the force from the rotors $\mathbf{F}_m^b$ with the total moments produced by the rotors $\mathbf{T}_m^b$, the relationship between the control inputs and actuator outputs (the control allocation or mixer as depicted in Fig. 3) can be expressed as $\mathbf{U} = \mathbf{M}\boldsymbol{\Omega}$ where

$$\mathbf{M} = \begin{bmatrix} -\frac{\sqrt{3}}{2}k_t & \frac{\sqrt{3}}{2}k_t & 0 & 0 & 0 & 0 \\ \frac{1}{2}k_t & \frac{1}{2}k_t & -k_t & 0 & 0 & 0 \\ 0 & 0 & 0 & -k_t & -k_t & -k_t \\ -\frac{\sqrt{3}}{2}k_d & \frac{\sqrt{3}}{2}k_d & 0 & -\frac{\sqrt{3}}{2}k_t l_0 & \frac{\sqrt{3}}{2}k_t l_0 & 0 \\ \frac{1}{2}k_d & \frac{1}{2}k_d & -k_d & \frac{1}{2}k_t l_0 & \frac{1}{2}k_t l_0 & -k_t l_0 \\ k_t l_0 & k_t l_0 & k_t l_0 & -k_d & -k_d & -k_d \end{bmatrix}$$

and $\mathbf{U} = \begin{bmatrix} \mathbf{F}_m^b & \mathbf{T}_m^b \end{bmatrix}^\top$.

3.2 Rigid-body model

Let $\boldsymbol{\xi}^e$ and $\boldsymbol{\omega}^b$ be the 3D positions and angular velocities respectively. The translational dynamics of a multi-tilt tricopter are given by (obtained by applying the Newton-Euler methods [37])

$$\ddot{\boldsymbol{\xi}}^e = \left[\boldsymbol{R}_e^b(\boldsymbol{\eta})^\top \mathbf{F}_m^b + \mathbf{F}_g^e\right]/m. \tag{7}$$

Similarly, the rotational dynamics can be derived as (following the techniques reported in [29])

$$\dot{\boldsymbol{\eta}} = \boldsymbol{\Gamma}\boldsymbol{\omega}^b, \tag{8}$$

where $\boldsymbol{\Gamma}$ is defined in (2). The angular acceleration vector is given by [37]

$$\dot{\boldsymbol{\omega}}^b = \mathbf{J}^{-1}\left[(-\boldsymbol{\omega}^b \times \mathbf{J}\boldsymbol{\omega}^b) + \mathbf{T}_t^b\right] \tag{9}$$

where $\mathbf{J} \triangleq \text{diag}\{J_x, J_y, J_z\}$ is the inertia matrix. At a steady hovering condition where the attitude angles and their rates are close to zero (commonly known as *small-angle approximation* in the literature, that is, if the variation of θ is assumed small, then $\sin(\theta) \approx \theta$, $\cos(\theta) \approx 1$ and $\dot{\theta} \approx 0$), the equations of motion of the tricopter (7), (8) and (9) reduce to a double integrator dynamics which inherently satisfies the NI property. This is one of the motivations for applying NI theory to the tricopter system. Note that the small-angle-approximation-based modelling technique yields similar results to a feedback-linearized model (of a trirotor or quadrotor). However, the latter may fail because it relies on cancelling the plant nonlinearities by multiplying them by their inverse terms. Mathematically derived inverses may not exactly match the dynamics due to inaccuracies in the real-time parameter identification process or parameter variation.

3.3 Tricopter hovering control using SMC

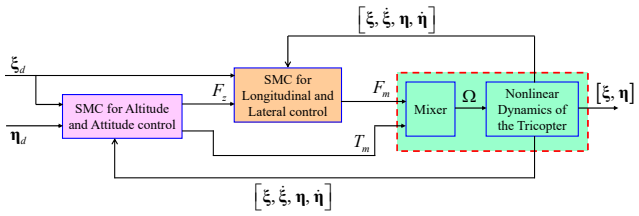

Fig. 3. A Sliding Mode Control scheme for the multi-tilt tricopter used to ensure stable hovering.

Assuming that the variation of the angles ϕ and θ are small, we have $\mathbf{\Gamma} \approx \boldsymbol{I}_3$ from (2), which implies $\ddot{\boldsymbol{\eta}} = \dot{\boldsymbol{\omega}}^b$ from (8). Upon expanding, (9) yields

$$\ddot{\phi} = \big[(J_y - J_z)\dot{\theta}\dot{\psi} + \tau_\phi\big]/J_x, \tag{10}$$
$$\ddot{\theta} = \big[(J_z - J_x)\dot{\phi}\dot{\psi} + \tau_\theta\big]/J_y, \tag{11}$$
$$\ddot{\psi} = \big[(Ix - Iy)\dot{\phi}\dot{\theta} + \tau_\psi\big]/J_z. \tag{12}$$

The approximation $\mathbf{\Gamma} = \boldsymbol{I}_3$ is typically used in the literature [31], [15], [6], etc., to obtain a simplified yet reasonably accurate model without sacrificing the crucial system properties.

We first consider the roll dynamics (10) and aim to design an SMC law for it. Exploiting the classical SMC theory [14], we choose an attractive sliding surface $\tilde{s}_\phi = \dot{e}_\phi + \lambda_\phi e_\phi$ where $e_\phi \triangleq \phi - \phi_d$ and $\lambda_\phi > 0$. We shall select the control law so that $\dot{\tilde{s}}_\phi = -k_\phi \operatorname{sgn}(\tilde{s}_\phi)$ with $k_\phi > 0$ such that $\tilde{s}_\phi \dot{\tilde{s}}_\phi \leq 0$. A standard Lyapunov candidate function $V_\phi = \frac{1}{2}\tilde{s}_\phi^2 > 0$ for all $\tilde{s}_\phi \neq 0$ is taken to analyse the stability of the sliding surface. We then calculate $\dot{V}_\phi$ as

$$\dot{V}_\phi = \tilde{s}_\phi \dot{\tilde{s}}_\phi = \tilde{s}_\phi(-k_\phi \operatorname{sgn}(\tilde{s}_\phi)) = -k_\phi|\tilde{s}_\phi| \leq 0 \tag{13}$$

where

$$\operatorname{sgn}(\tilde{s}) \triangleq \frac{|\tilde{s}|}{\tilde{s}} = \begin{cases} -1 & \tilde{s} < 0, \\ 0 & \tilde{s} = 0, \\ 1 & \tilde{s} > 0. \end{cases}$$

Using the relation $\tilde{s}_\phi \dot{\tilde{s}}_\phi = -k_\phi|\tilde{s}_\phi|$, we can readily find

$$\tilde{s}_\phi\Big(\frac{1}{J_x}\big[(J_y - J_z)\dot{\theta}\dot{\psi} + \tau_\phi\big] - \ddot{\phi}_d + \lambda_\phi \dot{e}_\phi\Big) = -k_\phi|\tilde{s}_\phi| \tag{14}$$

by substituting the expression of $\ddot{\phi}$ from (10). It gives

$$\tau_\phi = J_x\big(-k_\phi \operatorname{sgn}(\tilde{s}_\phi) + \ddot{\phi}_d - \lambda_\phi \dot{e}_\phi\big) - (J_y - J_z)\dot{\phi}\dot{\psi} \triangleq u_\phi. \tag{15}$$

Since $V_\phi > 0\ \forall \tilde{s}_\phi \neq 0$ and $\dot{V}_\phi \leq 0$, $\dot{V}_\phi = 0$ only when $\tilde{s}_\phi = 0$, that is, $\dot{e}_\phi + \lambda_\phi e_\phi = 0$. Therefore, the error dynamics $\dot{e}_\phi$ is asymptotically stable [14] as $\lambda_\phi > 0$. It implies $\lim_{t\to\infty} \phi(t) = \phi_d$ under the action of τ_ϕ. Following the above procedure, we can choose another two sliding surfaces $\tilde{s}_\theta = \dot{e}_\theta + \lambda_\theta e_\theta$ where $e_\theta \triangleq \theta - \theta_d$ and $\tilde{s}_\psi = \dot{e}_\psi + \lambda_\psi e_\psi$ where $e_\psi \triangleq \psi - \psi_d$ and obtain

$$\tau_\theta = J_y\big(-k_\theta \operatorname{sgn}(\tilde{s}_\theta) + \ddot{\theta}_d - \lambda_\theta \dot{e}_\theta\big) - (J_z - J_x)\dot{\theta}\,\dot{\psi} \triangleq u_\theta \tag{16}$$

for controlling the pitch motion and

$$\tau_\psi = J_z\big(-k_\psi \operatorname{sgn}(\tilde{s}_\psi) + \ddot{\psi}_d - \lambda_\psi \dot{e}_\psi\big) - (J_x - J_y)\dot{\phi}\,\dot{\theta} \triangleq u_\psi \tag{17}$$

for controlling the yaw motion.

Table 1
Summary of tricopter parameters

Parameter	Value
l_0	0.33 m
m	1.448 kg
k_t	1.084×10^{-5} kg-m
k_d	1.726×10^{-7} kg-m^2
J_x	1.035×10^{-1} kg-m^2
J_y	1.03×10^{-1} kg-m^2
J_z	1.709×10^{-1} kg-m^2

We make the following assumptions for the translational dynamics (7). During vertical motion, $\Sigma F_z \neq 0$, $\Sigma F_x = \Sigma F_y = 0$; during longitudinal motion, $\Sigma F_y = 0$, $\Sigma F_x \neq 0$, $\Sigma F_z \neq 0$; and during lateral motion, $\Sigma F_y \neq 0$, $\Sigma F_x = 0, \Sigma F_z \neq 0$. Along the translational axes, $F_z \neq 0$ because the vertical thrust is required to hold the altitude. Expanding (7) and imposing these simplifying assumptions, we get

$$\ddot{x} = \big[(c_\theta c_\psi)F_x + (c_\phi s_\theta c_\psi + s_\phi s_\psi)F_z\big]/m, \tag{18}$$
$$\ddot{y} = \big[(s_\phi s_\theta s_\psi + c_\phi c_\psi)F_y + (c_\phi s_\theta s_\psi - s_\phi c_\psi)F_z\big]/m, \tag{19}$$
$$\ddot{z} = g + \big[(c_\phi c_\theta)F_z\big]/m. \tag{20}$$

Similar to the attitude control cases, we choose $\tilde{s}_x = \dot{e}_x + \lambda_x e_x$, $\tilde{s}_y = \dot{e}_y + \lambda_y e_y$, $\tilde{s}_z = \dot{e}_z + \lambda_z e_z$ with $\lambda_x > 0$, $\lambda_y > 0$, $\lambda_z > 0$ and we get the sliding-mode control laws for the x, y and z motions:

$$F_x = \big[m\big(-k_x \operatorname{sgn}(\tilde{s}_x) + \ddot{x}_d - \lambda_x \dot{e}_x\big) - F_z(c_\phi s_\theta c_\psi + s_\phi s_\psi)\big]/c_\phi c_\psi \triangleq u_x, \tag{21}$$
$$F_y = \big[m\big(-k_y \operatorname{sgn}(\tilde{s}_y) + \ddot{y}_d - \lambda_y \dot{e}_y\big) - F_z(c_\phi s_\theta s_\psi - s_\phi c_\psi)\big]/(s_\phi s_\theta s_\psi + c_\phi c_\psi) \triangleq u_y, \tag{22}$$
$$F_z = \big[m\big(-k_z \operatorname{sgn}(\tilde{s}_z) - g + \ddot{z}_d - \lambda_z \dot{e}_z\big)\big]/c_\phi c_\theta \triangleq u_z. \tag{23}$$

Fig. 3 shows a schematic of the proposed SMC scheme for controlling attitude (η) and position (ξ) of a multi-tilt tricopter. For simulation purposes, $\lambda_x = \lambda_y = \lambda_z =$

$1.4, \lambda_\phi = \lambda_\theta = \lambda_\psi = 1.3, k_x = k_y = 1, k_z = 1.5$ and $k_\phi = k_\theta = k_\psi = 2.5$ are taken and the tricopter parameter values are listed in Table 1. Fig. 4 and Fig. 5 show the responses of the multi-tilt tricopter to a commanded (or reference) spiral trajectory with zero attitude change. Note that the tricopter under consideration can achieve independent x and y motions (6-DOF) without changing its attitude due to its airframe configuration.

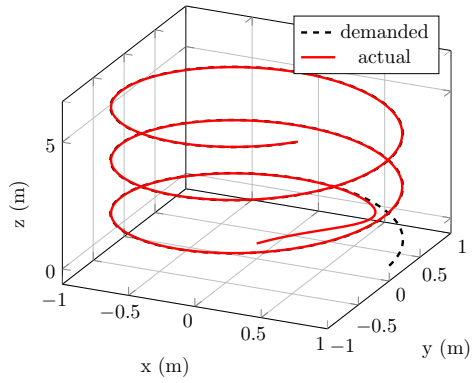

Fig. 4. Tricopter response to a spiral trajectory with SMC.

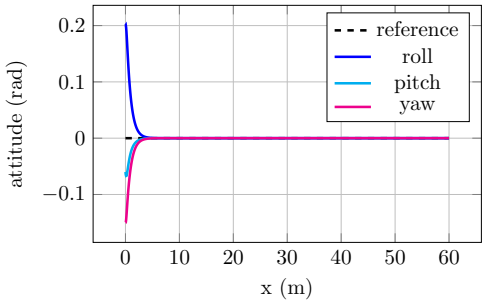

Fig. 5. Attitude profile exhibited during the simulation.

4 Subspace-based closed-loop system identification of a tricopter in the time-domain

This subsection focuses on developing a subspace-based closed-loop system identification technique in the continuous time domain to identify a linear model of the tricopter under a stable hovering condition achieved by the SMC scheme shown in Fig. 3. This technique also ensures that the identified linear model is NI by embedding the NI constraints [$AP + PA^\top \leq 0$ and $B + APC^\top = 0$ from Lemma 1] within the system identification algorithm. The idea has been inspired by [38] and [39], which showed that a quadcopter in a stable hovering condition, achieved under the action of a forward-path PID controller, exhibits NI properties. This work has first implemented an inner-loop SMC scheme (see Fig. 3 and Fig. 9) on the tricopter to ensure stable hovering. The sliding surface was chosen as $\tilde{s} = \dot{e} + \lambda e$ for each of the six channels as described in Section 3.3. The map from $[\xi_d^T \;\; \eta_d^T]^T$ to $[\xi^T \;\; \eta^T]^T$ in Fig. 3 should be close to unity at low frequencies under the action of the inner-loop SMC controller. However, at mid-to-high frequencies, noise will drive the inner loop away from the sliding surface, resulting in a lack of perfect tracking. Since the output will nonetheless still broadly follow the input with some additional phase lag, we expect the closed-loop dynamics from $[\xi_d^T \;\; \eta_d^T]^T$ to $[\xi^T \;\; \eta^T]^T$ in Fig. 3 to have NI properties.

4.1 Subspace-based closed-loop system identification in the continuous time domain

Since we need a system identification technique to identify an NI model of a multi-tilt tricopter, as described above, the NI constraints (3) given in Lemma 1 must to be imposed. These constraints are defined in the time domain via state-space matrices, which says subspace-based system identification can be a good choice. However, subspace-based system identification is generally performed in the discrete-time domain. If we transform conditions (3) to discrete-time equivalents, as done in [22] for instance, conditions (3) become non-convex and are no longer LMIs, making the identification process more complex and less intuitive. To overcome this issue, we propose a continuous-time version of the existing subspace-based system identification technique utilizing the ideas of [9], [26] and [8]. It is worth noting that the proposed system identification technique is implemented on the inner-loop-SMC-controlled tricopter. Open-loop system identification is too difficult in the current situation because the tricopters are open-loop unstable.

Consider a minimal state-space realization (A, B, C, D) of a SISO, real, rational, proper transfer function $M(s)$ where $A \in \mathbb{R}^{n\times n}, B \in \mathbb{R}^{n\times 1}, C \in \mathbb{R}^{1\times n}, D \in \mathbb{R}^{1\times 1}$, $x(t) \in \mathbb{R}^n$, $u(t) \in \mathbb{R}$ and $y(t) \in \mathbb{R}$ for all $t \geq 0$. For a continuous-time LTI system, the output $y(t)$ can be expressed as [1]

$$y(t) = \mathscr{L}^{-1}[Y(s)] = \mathscr{L}^{-1}\big[\{C(sI - A)^{-1}B + D\}U(s)\big]$$
$$= C\int_0^t e^{A(t-\tau)}Bu(\tau)\,\mathrm{d}\tau + Du(t). \qquad (24)$$

For a strictly-proper ($D = 0$) system, (24) can be rearranged as $y(t) = C\big\{\int_0^t e^{A(t-\tau)}u(\tau)\,\mathrm{d}\tau\big\}B$ since the system $M(s)$ is SISO.

The proposed system identification process is described below through three main steps. The estimated A, B and C matrices will be denoted by $\hat{A}$, $\hat{B}$ and $\hat{C}$.

Step 1: The Laguerre Filter algorithm in [8] is used to generate filtered input-output data sets from experimentally observed data sets;

[1] The notation $\mathscr{L}^{-1}(\cdot)$ stands for the Laplace inverse.

Step 2: The error-in-variables family of subspace algorithms [26] is used to estimate the $\hat{A}$ and $\hat{C}$ matrices of the system relying on the filtered input-output data sets generated in Step 1;

Step 3: The column vector $\hat{B}$ is constructed by solving the least squares optimization problem (27) which uses the estimated $\hat{A}$ and $\hat{C}$ matrices (from Step 2).

The readers are referred to [26] and [8] to review the estimation algorithm (for finding $\hat{A}$ and $\hat{C}$), which we have utilised in Steps 1 and 2. In this paper, Step 3 is modified by embedding the NI constraints (from Lemma 1) to enforce the NI property of the identified model.

For a SISO channel of a strictly proper LTI system, if we pack the measured input-output time-series data in $\mathbf{u} = [u(t_1),\ u(t_2),\ \cdots,\ u(t_N)]^\top \in \mathbb{R}^{N\times 1}$ and $\mathbf{y} = [y(t_1),\ y(t_2),\ \cdots,\ y(t_N)]^\top \in \mathbb{R}^{N\times 1}$ where N data points have been collected in the time interval $[0, t_N]$, we can express $\mathbf{y}$ as

$$\begin{bmatrix} y(t_1) \\ y(t_2) \\ \vdots \\ y(t_N) \end{bmatrix} = \begin{bmatrix} \hat{C}\big\{\int_0^{t_1} e^{\hat{A}(t_1-\tau)}u(\tau)\,\mathrm{d}\tau\big\}\hat{B} \\ \hat{C}\big\{\int_0^{t_2} e^{\hat{A}(t_2-\tau)}u(\tau)\,\mathrm{d}\tau\big\}\hat{B} \\ \vdots \\ \hat{C}\big\{\int_0^{t_N} e^{\hat{A}(t_N-\tau)}u(\tau)\,\mathrm{d}\tau\big\}\hat{B} \end{bmatrix}, \tag{25}$$

which can be expressed in a vector-matrix form as $\mathbf{y} = \mathbf{\Phi}\hat{B}$ where $\mathbf{\Phi} \in \mathbb{R}^{N\times n}$ and $\hat{B} \in \mathbb{R}^{n\times 1}$. The matrix $\mathbf{\Phi}$ is known for a known input function $u(t)$ over all $t \in [0, t_N]$. However, since $\mathbf{\Phi}$ involves integrals and our measured input contains discrete-time data points $\{u(t_1),\ u(t_2),\ \cdots,\ u(t_N)\}$, we can use a numerical integration technique such as a first-order approximation of an integral (or Trapezoidal rule, or Simpson's rule, etc.) to calculate $\mathbf{\Phi}$.

Finally, imposing the NI constraint $\hat{B} = -\hat{A}P\hat{C}^\top$ from (3) into $\mathbf{y} = \mathbf{\Phi}\hat{B}$, we have

$$\mathbf{y} = -\mathbf{\Phi}\hat{A}P\hat{C}^\top \tag{26}$$

where $P = P^\top > 0$ is the unknown matrix variable to be determined. Equation (26) can be solved for $P > 0$ satisfying $\hat{A}P + P\hat{A}^\top \leq 0$ via the following constrained least-squares minimization problem:

$$\begin{aligned} &\min_{P} \ \left\| \mathbf{\Phi}^\top\mathbf{y} + \mathbf{\Phi}^\top\mathbf{\Phi}\hat{A}P\hat{C}^\top \right\|^2 \\ &\text{subject to} \\ &\hat{A}P + P\hat{A}^\top \leq 0 \text{ and } P = P^\top > 0, \end{aligned} \tag{27}$$

using techniques in [21]. The objective function in (27) is quadratic in P, and the constraints are affine in P. Thus, it is a convex optimization problem that can be conveniently solved using commercially available SDP solver packages (e.g. CVX, SeDuMi, Yalmip, etc.). Once P is obtained, $\hat{B}$ is computed as $\hat{B} = -\hat{A}P\hat{C}^\top$.

4.2 System identification of an inner-loop-SMC-controlled tricopter enforcing NI property

In this subsection, the linearized multi-tilt tricopter from Section 3.3 with six inputs $(x_d, y_d, z_d, \phi_d, \theta_d, \psi_d)$ and their respective outputs is considered as the closed-loop system to be identified. The input-output data is obtained by exciting each channel with a square wave and measuring the corresponding output signal. The continuous time identification algorithm described in Section 4.1 is then used to identify a model for each channel. The Laguerre filter gain p for each channel was heuristically chosen as $0.55, 0.45, 0.34, 0.35, 0.4$ and 0.45 respectively, and by inspecting the singular values in the identification process, the model order was chosen as $n = 2$ for all channels, yielding the following SISO NI transfer functions for the respective channels:

$$m_1(s) = \frac{X(s)}{X_d(s)} = \frac{2.3662\times 10^{-5}s + 3.515\times 10^{-5}}{s^2 + 0.006301s + 4.357\times 10^{-5}}, \tag{28}$$

$$m_2(s) = \frac{Y(s)}{Y_d(s)} = \frac{2.659\times 10^{-14}s + 2.714\times 10^{-5}}{s^2 + 0.006625s + 3.682\times 10^{-5}}, \tag{29}$$

$$m_3(s) = \frac{Z(s)}{Z_d(s)} = \frac{8.769\times 10^{-14}s + 2.38\times 10^{-5}}{s^2 + 0.006368s + 3.067\times 10^{-5}}, \tag{30}$$

$$m_4(s) = \frac{\Phi(s)}{\Phi_d(s)} = \frac{6.114\times 10^{-17}s + 4.827\times 10^{-5}}{s^2 + 0.01231s + 5.206\times 10^{-5}}, \tag{31}$$

$$m_5(s) = \frac{\Theta(s)}{\Theta_d(s)} = \frac{7.62\times 10^{-14}s + 5.676\times 10^{-5}}{s^2 + 0.01357s + 5.849\times 10^{-5}}, \tag{32}$$

$$m_6(s) = \frac{\Psi(s)}{\Psi_d(s)} = \frac{1.419\times 10^{-14}s + 1.49\times 10^{-4}}{s^2 + 0.003192s + 1.325\times 10^{-4}}, \tag{33}$$

where $X(s)$, $Y(s)$, $Z(s)$, $\Phi(s)$, $\Theta(s)$ and $\Psi(s)$ denote the Laplace transform of the real-time physical variables $x(t)$, $y(t)$, $z(t)$, $\phi(t)$, $\theta(t)$ and $\psi(t)$ respectively. Equations (28)–(33) together represent the inner-loop-SMC-controlled dynamics of the multi-tilt tricopter in the closed loop with six inputs and six outputs. Figures 6–8 show the frequency response validation of the identified models together with a comparison of these models with the classic subspace identification algorithm [41] and [21]. In Figures 6–8, *unconstrained* refers to the classic subspace algorithm [41] while *constrained* refers to our proposed continuous-time algorithm, which solves the constrained optimization problem (27) and guarantees that the identified model is NI. It is evident from Figures 6–8 that the identified models for each channel using the proposed algorithm have a phase in the range $[-\pi, 0]$, which is required for a negative imaginary system. Furthermore, it can also be observed from Figures 6–8 that for all channels except roll and yaw, the proposed algorithm (constrained) yields better fits with

the validation data compared to the classic subspace algorithm (unconstrained).

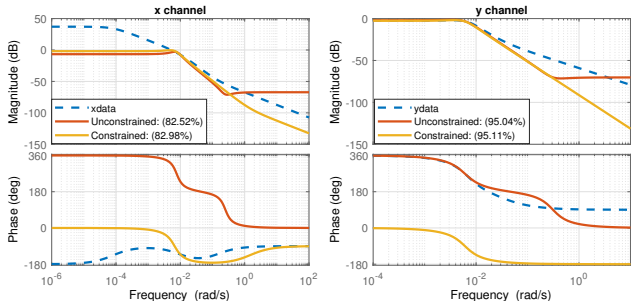

Fig. 6. Frequency response comparison: x and y channels

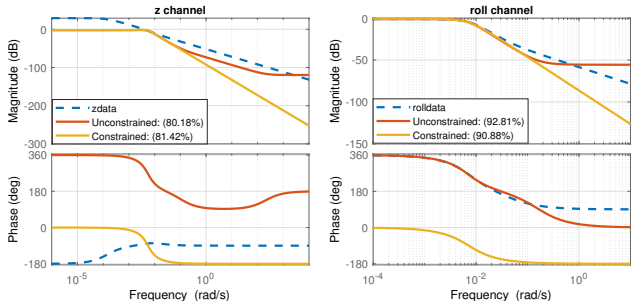

Fig. 7. Frequency response comparison: z and roll channels

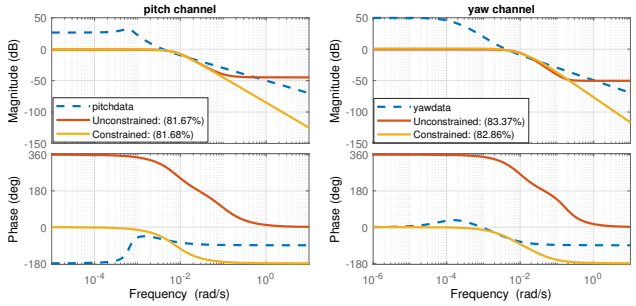

Fig. 8. Frequency response comparison: pitch and yaw channels

5 A distributed two-loop formation control scheme for networked multi-tilt tricopters

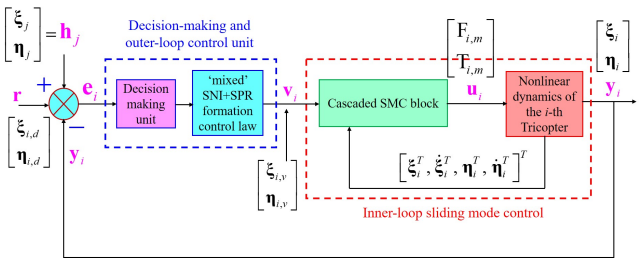

Fig. 9. A two-loop formation control scheme for networked multi-tilt tricopters using an inner-loop cascaded SMC block and outer-loop distributed 'mixed' SNI+SPR control law.

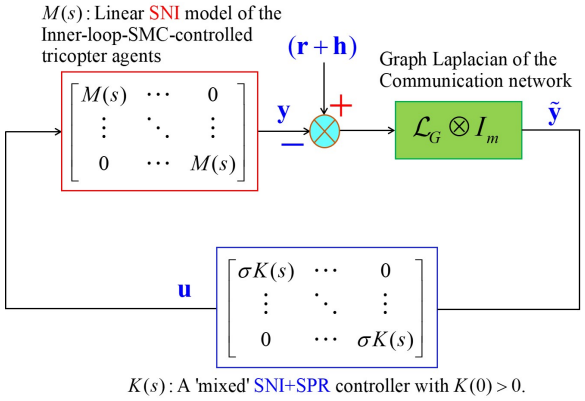

Fig. 10. The outer-loop formation control scheme for a group of networked inner-loop-SMC-controlled tricopter agents $M(s)$ (being SNI) utilising a distributed output feedback 'mixed' SNI+SPR controller $K(s)$ with $K(0) > 0$.

This section lays down the foundational results which underpin the main contributions of this paper that will be developed in the subsequent sections. Here, we will establish that a network of inner-loop-SMC-controlled agents can be made closed-loop stable via a distributed 'mixed' SNI+SPR controller depending only on the sign definiteness of the DC-gain matrix of the controller transfer function. This result will be invoked later to develop a leader-following formation control scheme (shown in Fig. 10) for networked inner-loop-SMC-controlled multi-tilt tricopter agents.

5.1 *Closed-loop stability of networked stable NI/SNI system with a 'mixed' SNI+SPR controller*

In this subsection, we will first establish (in Lemma 2) that a network of inner-loop-SMC-controlled multi-tilt tricopter agents $M(s) = \text{diag}\{m_1(s), m_2(s), \ldots, m_m(s)\}$ as derived in (28))–(33), being stable NI/SNI with $M(0) > 0$, connected via an undirected graph, can be stabilized in a negative feedback loop shown in Fig. 10 by a distributed 'mixed' SNI+SPR controller $K(s)$ having $K(0) > 0$. The terminology 'mixed' SNI+SPR controller signifies that the elements of $K(s)$ exhibit either purely SNI property, purely SPR property, or a *mixture* of SNI and SPR properties. In other words, some elements of $K(s)$ may be SNI, some may be SPR, while the rest satisfy SNI and SPR properties. Theorem 2 is the main contribution of this section, which proves that a group of networked multi-tilt tricopter agents achieves a predefined time-invariant or time-varying formation under the application of a distributed 'mixed' SNI+SPR controller $K(s)$, described before when $K(0) > 0$. Lemma 2 is an essential technical prerequisite result, which will be invoked for proving Theorem 2. The proof of Lemma 2 significantly relies on the Characteristic loci theory [2], [24] and has been done taking the inspiration from [4] and [12].

Lemma 2 *Consider a network of N identical and decou-*

pled NI/SNI systems $M(s) \in \mathscr{RH}_\infty^{m\times m}$ with $M(0) > 0$. Let the graph $\mathscr{G}$ be associated with a network satisfying Assumption 1. Then, there exists a finite range of $\sigma \in (0, \sigma^\star]$ for which the negative feedback interconnection of $[\mathscr{L}_G \otimes \sigma K(s)]$ and $M(s)$ shown in Fig. 11 remains asymptotically stable where $K(s) \in \mathscr{RH}_\infty^{m\times m}$ is a decoupled, 'mixed' SNI+SPR system satisfying $K(0) > 0$.

Proof. In this proof, the notation $\rho_i(s)$ is used to represent the characteristic loci of the networked loop transfer function matrix $[\mathscr{L}_G \otimes K(s)M(s)]$. To apply the characteristic loci technique, we will define the following two sets of the complex variable s

$$\Omega_{\pm j} = \{s|\ s = j\omega,\ \omega \in (-\infty, \infty)\},$$
$$\Omega_R = \{s|\ s = Re^{j\theta},\ R \in \mathbb{R}_{>0}, R \to +\infty,\ -\frac{\pi}{2} \le \theta \le \frac{\pi}{2}\},$$

along the s-plane $\mathscr{D}$-contour shown in Fig. 12b. The negative feedback interconnection of $M(s)$ and $[\mathscr{L}_G \otimes K(s)]$, as shown in Fig. 11, remains asymptotically stable if none of the characteristic loci $\rho_i(j\omega)$ encircles the critical point $(-\frac{1}{\sigma} + j0)$ for any $\sigma \in (0, \sigma^\star]$ via Theorem 1. We will now establish via the following two parts (Parts I and II) that all the characteristic loci $\rho_i(s)$ remain confined within the Green-coloured region portrayed in Fig. 12a. Before starting the proof, we note that both $M(s) \in \mathscr{RH}_\infty^{m\times m}$ and $K(s) \in \mathscr{RH}_\infty^{m\times m}$ have decoupled structures, that is, $M(s) = \text{diag}\{m_1(s), m_2(s), \cdots, m_m(s)\}$ and $K(s) = \text{diag}\{k_1(s), k_2(s), \cdots, k_m(s)\}$. Since $M(s)$ is stable NI/SNI and $K(s)$ is 'mixed' SNI+SPR respectively, $\angle m_i(j\omega) \in [-\pi, 0]$ and $\angle k_i(j\omega) \in (-\pi, \frac{\pi}{2})$ $\forall \omega \in (0, \infty)$ and $\forall i \in \{1, 2, \ldots, m\}$. Also, $\angle m_i(0) = 0$ and $\angle k_i(0) = 0$ $\forall i$ since $M(0) = M(0)^\top > 0$ and $K(0) = K(0)^\top > 0$ via supposition and due to satisfying the stable NI/SNI properties. We also assume that $[M(s) - M^\sim(s)]$ has full normal rank.

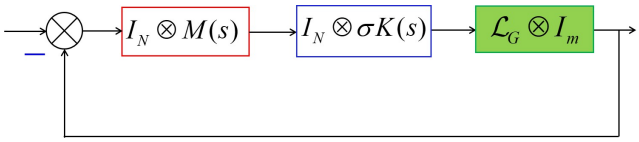

Fig. 11. A rearranged block diagram of the scheme shown in Fig. 10 required for closed-loop stability analysis.

Part I: When $s \in \Omega_{\pm j}$ [i.e. when $\omega \in (-\infty, \infty)$]

Let $\lambda_i[\mathscr{L}_G \otimes K(j\omega)M(j\omega)] = \lambda_i[\mathscr{L}_G]\,|k_i(j\omega)||m_i(j\omega)|\, e^{j(\phi_i+\psi_i)}$ at each $\omega \in (0, \infty)$ and $\forall i \in \{1, 2, \ldots, Nm\}$. Since $M(s)$ is stable NI and $K(s)$ is 'mixed' SNI+SPR, $\psi_i(\omega) \in [-\pi, 0]$ and $\phi_i(\omega) \in (-\pi, \frac{\pi}{2})$ $\forall \omega \in (0, \infty)$ and hence, $\angle\rho_i(j\omega) = (\phi_i(\omega) + \psi_i(\omega)) \in (-2\pi, 0]$ $\forall \omega \in (0, \infty)$ $\forall i$. Similarly, $\forall \omega \in (-\infty, 0)$, $\angle\rho_i(j\omega) \in (-2\pi, 0]$. At $\omega = 0$, we have $\lambda_i[\mathscr{L}_G \otimes K(0)M(0)] = \lambda_i[\mathscr{L}_G]\,|k_i(0)||m_i(0)|\angle 0$ as $K(0) > 0$ and $M(0) > 0$.

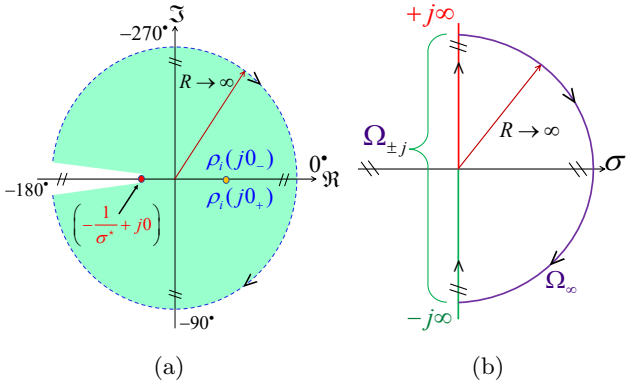

Fig. 12. (a) All the characteristic loci $\rho_i(j\omega)$ of $\mathscr{L}_G \otimes K(s)M(s)$ remain inside the Green coloured region for any $\sigma \in (0, \sigma^\star]$ and $\forall \omega \in \mathbb{R} \cup \{\infty\}$. $(-\frac{1}{\sigma^\star} + j0)$ denotes the worst-case critical point (i.e. when $\sigma = \sigma^\star$); (b) Nyquist $\mathscr{D}$-contour in the s-plane without any pole on the $j\omega$ axis.

Therefore, the zero-frequency points $\rho_i(j0_-)$ and $\rho_i(j0_+)$ lie on the positive real axis of the characteristic loci plane, and they coincide as $K(s)M(s)$ does not have any pole(s) at the origin. Thus, when $s \in \Omega_{\pm j}$, the angle contribution $\angle\rho_i(j\omega)$ of each $\rho_i(j\omega)$ belongs to the range $[-2\pi, 0]$ $\forall \omega \in \mathbb{R}$. Most importantly, there is no infinite crossover on the negative or positive real axis as $K(s)M(s)$ does not have any pole at $s = 0$. However, the characteristic loci $\rho_i(s)$ may intersect the negative real axis one or multiple times at finite distances since the intercept, given by $\lambda_i[\mathscr{L}_G]\,|k_i(j\omega)||m_i(j\omega)|$, remains finite at all $\omega \in \mathbb{R}$. These two arguments together imply that there always exists a finite range $(0, \sigma^\star]$ of the parameter σ for which the critical point $(-\frac{1}{\sigma} + j0)$ is never encircled by any $\rho_i(j\omega)$. The fact has been graphically demonstrated in Fig. 12a. It shows that all $\rho_i(j\omega)$ stay within the Green coloured region such that the critical point $(-\frac{1}{\sigma} + j0)$ is never encircled for any $\sigma \in (0, \sigma^\star]$.

Part II: When $s \in \Omega_R$ Similar to the zero-frequency points $\rho_i(j0_-)$ and $\rho_i(j0_+)$, the infinite frequency points $\rho_i(+j\infty)$ and $\rho_i(-j\infty)$ can be expressed as $\lambda_i[\mathscr{L}_G \otimes K(\infty)M(\infty)] = \lambda_i[\mathscr{L}_G]\,|k_i(\infty)||m_i(\infty)|\angle(\phi_i(\infty) + \psi_i(\infty))$ $\forall i \in \{1, 2, \ldots, Nm\}$. Since the eigenvalues of $K(\infty)M(\infty)$ are always real numbers (positive/negative/zero), $\lambda_i[\mathscr{L}_G] > 0$ $\forall i$ and neither of $K(s)$ and $M(s)$ contains a pole at the origin, $\rho_i(+j\infty)$ and $\rho_i(-j\infty)$ coincide and lie either at the origin or on the real axis at finite distances from the origin. Combining all these arguments, we can conclude that there always exists a finite range $(0, \sigma^\star]$ of the gain parameter σ for which none of the characteristic loci $\rho_i(j\omega)$ encircles the critical point $(-\frac{1}{\sigma} + j0)$ for the entire frequency range $\omega \in \mathbb{R} \cup \{\infty\}$ [this has been demonstrated in Fig. 12a, which shows that all $\rho_i(s)$ remain within the Green coloured region and the worst-case critical point $(-\frac{1}{\sigma^\star} + j0)$ also lies outside the Green coloured region].

Parts I and II together prove that all the characteristic

loci $\rho_i(s)$ of the loop transfer function $[\mathscr{L}_G \otimes K(s)M(s)]$ remain within the Green coloured region shown in Fig. 12a and hence, none of the characteristic loci $\rho_i(s)$ encircles the critical point $(-\frac{1}{\sigma}+j0)$ for any $\sigma \in (0, \sigma^\star]$. This proves the asymptotic stability of the negative feedback closed-loop system shown in Fig. 11 exploiting Theorem 1.

Note that the same proof readily specialises to the cases when $M(s)$ belongs to the SNI class for which the full normal rank condition (i.e. $[M(s)-M^{\sim}(s)]$ has full normal rank) is inherently satisfied. Hence, the entire proof is done. ■

5.2 *Formation control protocol design using a 'mixed' SNI and SPR system property*

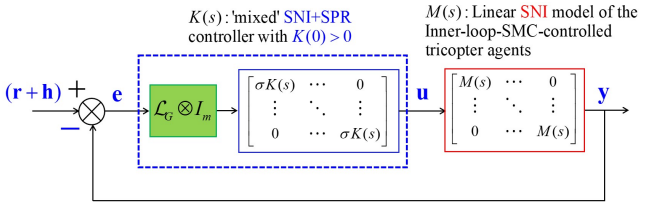

Fig. 13. An equivalent block diagram of the formation control scheme shown in Fig. 10 for inner-loop-SMC-controlled networked tricopter agents. Note $\mathscr{L}_G = (\mathscr{L} + \mathbb{G})$.

This subsection presents the key contribution of this paper. NI and PR theories have been exploited to design a simple yet effective formation control scheme as depicted in Fig. 10 for a class of UAVs that can be modelled as (or transformed into) a network of linearized dynamics. Although the formation control scheme developed in this section is meant for tricopter UAVs, it is also well-suited for other UAV configurations (e.g. quadcopter). In Theorem 2 and subsequent parts, the inner-loop-SMC-controlled dynamics of a multi-tilt tricopter is represented by $M(s) = \text{diag}\{m_1(s), m_2(s), \ldots, m_6(s)\} \in \mathscr{RH}_\infty^{6\times 6}$ with $M(0) > 0$, as derived in (28)–(33).

Theorem 2 *Consider a network of N identical inner-loop-SMC-controlled, multi-tilt tricopter agents $M(s) \in \mathscr{RH}_\infty^{m\times m}$, connected via the topology $\mathscr{G}$ that satisfies Assumption 1. Let $\mathbf{h}(t) = \left[\boldsymbol{h}_1^\top\ \boldsymbol{h}_2^\top, \ldots, \boldsymbol{h}_N^\top\right]^\top \in \mathbb{R}^{Nm}$ be the desired formation configuration vector and $\bar{\mathbf{r}} = \mathbf{1}_N \boldsymbol{r} \in \mathbb{R}^{Nm}$ be the formation reference vector. Let $K(s) \in \mathscr{RH}_\infty^{m\times m}$ be a decoupled, 'mixed' SNI+SPR controller satisfying $K(0) > 0$. Then, there always exists a finite $\sigma^\star > 0$ such that for any $\sigma \in (0, \sigma^\star]$ the tricopter agents achieve the desired formation with respect to $\mathbf{r}(t)$ and $\mathbf{h}(t)$ by the following distributed dynamic output feedback control law (according to the scheme shown in Fig. 10)*

$$\boldsymbol{u}_i = \sigma K(s) \sum_{j=1}^{N} a_{ij}\big((\boldsymbol{y}_j - \boldsymbol{h}_j) - (\boldsymbol{y}_i - \boldsymbol{h}_i)\big) + g_i(\boldsymbol{r} + \boldsymbol{h}_i - \boldsymbol{y}_i) \tag{35}$$

$\forall i \in \{1, 2, \ldots, N\}$.

Proof: We begin this proof by noting that the inner-loop-SMC-controlled model $M(s) \in \mathscr{RH}_\infty^{m\times m}$ of the multi-tilt tricopter, derived in (28)–(33), satisfies the SNI property with $M(0) > 0$. The proposed formation control scheme for networked multi-tilt tricopter agents is shown in Fig. 10. An equivalent block diagram of Fig. 10 has been drawn in Fig. 13 to assist the proof of Theorem 2. We denote $\mathscr{L}_G = \mathscr{L} + \mathbb{G}$. The proof builds on Lemma 2, which establishes the asymptotic stability of negative feedback closed-loop interconnection of a networked stable NI/SNI plant $(\mathscr{L}_G \otimes M(s))$ and a decoupled 'mixed' SNI+SPR controller $(I_N \otimes \sigma K(s))$ exploiting the characteristic loci technique (Theorem 1).

In Fig. 13, the Green dotted box represents the distributed 'mixed' SNI+SPR controller $\mathscr{L}_G \otimes \sigma K(s)$. For the proof, the network part (i.e. $\mathscr{L}_G = \mathscr{L} + \mathbb{G}$) has been decoupled from the plant and attached with the controller block. Now, the negative feedback interconnection of the inner-loop-SMC-controlled multi-tilt tricopter system $\bar{M}(s) = \text{diag}\{M(s), M(s), \cdots, M(s)\}$ and the networked controller $\mathscr{L}_G \otimes \sigma K(s)$, as shown in Fig. 13, is asymptotically stable for a finite range of $\sigma \in (0, \sigma^\star]$ via Lemma 2 as Fig. 11 is equivalent to Fig. 13. The asymptotic stability of the networked loop (i.e. the formation control scheme) ensures that the formation tracking error will asymptotically decay to zero, that is, $\lim_{t\to\infty} \mathbf{e}(t) = 0$ or $\lim_{t\to\infty} \mathbf{r}(t) + \mathbf{h}(t) - \mathbf{y}(t) = 0$. This part readily follows from Theorem 1 of [34] and [44]. Hence, we can conclude that the group of inner-loop-SMC-controlled multi-tilt tricopter agents will achieve the desired formation specified by $\mathbf{r}$ and $\mathbf{h}$ under the action of the distributed 'mixed' SNI+SPR output feedback control protocol (35) following the scheme shown in Fig. 10 [equivalently Fig. 13]. ■

Remark 1 *The negative feedback consensus-seeking scheme developed for inner-loop-SMC-controlled tricopter agents may be easily modified to cater to single and double-integrator agents. In that respect, the results presented in [11] and [12] where tricopters were feedback-linearized to single/double integrator systems can be captured by our scheme. However, it has been investigated that in the case of single integrator agents, if a negative feedback consensus scheme is used, then the requirement of an SNI controller can be relaxed to a stable NI (as opposed to an SNI) controller. This reduces the conservatism of the proposed consensus scheme and, hence, is worth detailed analysis.*

Remark 2 *It is worth noting that different from [12], our SNI+SPR controller is more generalized since it supports any NI system, including single and double integrator systems and their combinations. Also, the authors in [12] have considered the SISO case while proposing a cooperative control law, while we have considered the MIMO case, which also encompasses SISO systems. Furthermore, our SNI+SPR control law offers better transient performance than the SNI-only control law of [12] due to the inclusion of a phase lead (a zero) in the closed loop system, made possible by the strictly passive part of the controller. The inclusion of the passive part also means that our SNI+SPR control law is part of a wider set of controller transfer functions as the Nyquist plot lies not only below the real axis but within the first, third and fourth quadrants, providing a larger family of controller transfer functions compared to the SNI-only control law of [12].*

It is also worth noting that the proposed scheme (Theorem 2) can be readily extended to take up a group formation control problem, allowing multiple leaders.

6 Robustness and fault-tolerance properties

6.1 Robustness to model uncertainty

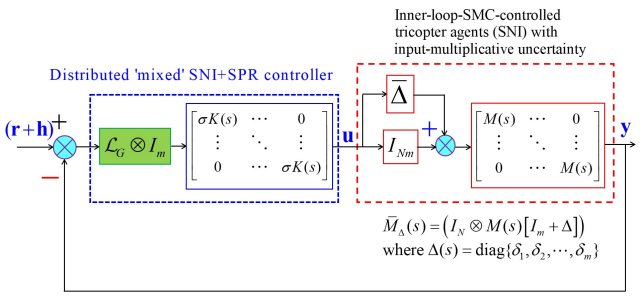

Fig. 14. A formation control scheme for inner-loop-SMC-controlled tricopter agents with a class of IM-type uncertainty $\delta_i \in \mathbf{U}\ \forall i$.

This subsection examines the robustness of the NI-based leader-following consensus scheme developed for distributed double integrator agents. This study is particularly motivated by the fact that many practical robotic systems can be feedback linearized into double integrator dynamics along with uncertain parts appearing in a multiplicative or an additive structure. We now declare a particular class of uncertainties $\Delta(s) = \text{diag}\{\delta_1(s), \delta_2(s), \cdots, \delta_m(s)\}$ where $\delta_i(s)$ belongs to a set $\mathbf{U}$ defined below:

$$\mathbf{U} = \Big\{\delta(s) \in \mathscr{RH}_\infty : -\pi \leq \angle\delta(j\omega) \leq \frac{\pi}{2}\ \ \forall \omega \in \mathbb{R}_{\geq 0} \text{ and } \delta(0) > 0\Big\}. \tag{36}$$

Note that the uncertainties are not restricted to the NI class. Theorem 3 given below will establish that the NI-based distributed leader-following consensus scheme offers robustness against **U**-type uncertainties when they appear with double integrator dynamics.

Theorem 3 *Consider a network of N identical multi-tilt tricopters having an uncertain inner-loop-SMC-controlled model given by $M_\Delta(s) = M(s)[I + \Delta(s)] \in \mathscr{RH}_\infty^{m\times m}$ where $M(s)$ is the nominal model (stable NI/SNI) and $\Delta(s) = \text{diag}\{\delta_1(s), \delta_2(s), \cdots, \delta_m(s)\}$ with $\delta_i \in \mathbf{U}\ \forall i$. The interaction topology $\mathscr{G}$ satisfies Assumption 1. Let $\mathbf{h}(t) = \left[\boldsymbol{h}_1^\top\ \boldsymbol{h}_2^\top, \cdots, \boldsymbol{h}_N^\top\right]^\top \in \mathbb{R}^{Nm}$ be the desired formation configuration vector and $\bar{\mathbf{r}} = \mathbf{1}_N \boldsymbol{r} \in \mathbb{R}^{Nm}$ be the formation reference vector. Let $K(s) \in \mathscr{RH}_\infty^{m\times m}$ be a decoupled, 'mixed' SNI+SPR controller satisfying $K(0) > 0$. Then, there always exists a finite $\sigma^\star > 0$ such that for any $(0, \sigma^\star]$, the tricopter agents achieve the desired formation with respect to $\mathbf{r}(t)$ and $\mathbf{h}(t)$ by the distributed 'mixed' SNI+SPR output feedback control law* (35) *following the scheme shown in Fig. 14.*

Proof. We will first establish the asymptotic stability of the formation control scheme (shown in Fig. 14) in the presence of a class input-multiplicative-type (IM-type) uncertainty $\Delta(s) = \text{diag}\{\delta_1(s), \delta_2(s), \cdots, \delta_m(s)\}$ where $\delta_i(s) \in \mathbf{U}\ \forall i \in \{1, 2, \ldots, m\}$. It is guaranteed that none of the eigenvalue loci $\rho_i(j\omega)$ of $\left[\mathscr{L}_G \otimes K(s)M_\Delta(s)\right]$, where $M_{\Delta(s)} = M(s)[I + \Delta(s)]$, encircles the worst-case critical point $(\frac{1}{\sigma^\star} + j0)$ for any $\delta(s) \in \mathbf{U}$. Let $M(s)$ be stable NI—the proof proceeds along the similar track of the proof of Theorem 2.

Part I: When $s \in \Omega_{\pm j}$ [i.e. when $\omega \in (-\infty, \infty)$]

Let $\lambda_i\left[\mathscr{L}_G \otimes K(j\omega)M_\Delta(j\omega)\right] = \lambda_i\left[\mathscr{L}_G\right]|k_i(j\omega)||m_i(j\omega)[1 + \delta_i(j\omega)]|e^{j(\phi_i(\omega)+\psi_i(\omega)+\nu_i(\omega))}$ at each $\omega \in (0, \infty)$ and $\forall i \in \{1, 2, \ldots, Nm\}$. Note $\phi_i(\omega) \in [-\pi, 0]$ as $M(s)$ is stable NI, $\psi_i(\omega) \in (-\pi, \frac{\pi}{2})$ as $K(s)$ is 'mixed' SNI+SPR and $\nu_i(\omega) \in [-\pi, \frac{\pi}{2}]$ for all $\omega \in \mathbb{R}_{\geq 0}$. At $\omega = 0$, $\phi_i(0) = \psi_i(0) = \nu_i(0) = 0$. Therefore, $(\phi_i(\omega) + \psi_i(\omega) + \nu_i(\omega)) \in [-\pi, \pi]\ \forall \omega \in \mathbb{R}_{\geq 0}$. Similarly, $\forall \omega \in (-\infty, 0)$, $(\phi_i(\omega) + \psi_i(\omega) + \nu_i(\omega)) \in [-\pi, \pi]$. It implies that the zero-frequency points $\rho_i(j0_-)$ and $\rho_i(j0_+)$ coincide and lie on the positive real axis for any $\delta \in \mathbf{U}$ since $K(s)M_\Delta(s)$ does not have any pole(s) at $s = 0$. Thus, when $s \in \Omega_{\pm j}$, the angle contribution $\angle\rho_i(j\omega)$ of each $\rho_i(j\omega)$ belongs to the range $[-\pi, \pi]\ \forall \omega \in \mathbb{R}$. Most importantly, there is no infinite crossover on the negative or positive real axis as $K(s)M_\Delta(s)$ does not have any pole at $s = 0$. However, $\rho_i(s)$ may intersect the negative real axis one or multiple times at finite distances since the intercept, given by $\lambda_i\left[\mathscr{L}_G\right]|k_i(j\omega)||m_i(j\omega)\ [1 + \delta_i(j\omega)]|$, remains finite at all $\omega \in \mathbb{R}$ and $\forall i \in \{1, 2, \ldots, Nm\}$. These two arguments together imply that there always exists a finite range of $\sigma \in (0, \sigma^\star]$ such that the worst-case critical point $(-\frac{1}{\sigma^\star} + j0)$ is never encircled by any $\rho_i(j\omega)$. The

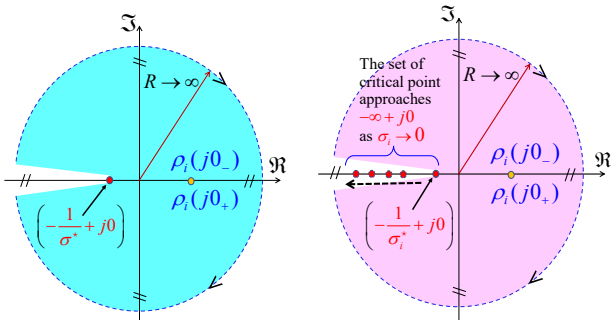

Fig. 15. (a) All the characteristic loci $\rho_i(j\omega)$ of $\mathscr{L}_G \otimes K(s)M_\Delta(s)$ remain inside the Cyan-coloured region for the full class of $\delta \in \mathbf{U}$; (b) The figure shows that the set of critical points approaches $(-\infty + j0)$ when $\sigma_i \to 0$. Note that $\sigma_i \in [0, \sigma_i^\star]$. This interprets the fault tolerance property.

fact has been graphically demonstrated in Fig. 15a. It shows that all $\rho_i(j\omega)$ stay within the Cyan-coloured region for any IM-type uncertainties $\delta(s) \in \mathbf{U}$.

Part II: When $s \in \Omega_R$ Similar to the zero-frequency points $\rho_i(j0_-)$ and $\rho_i(j0_+)$, the infinite frequency points $\rho_i(+j\infty)$ and $\rho_i(-j\infty)$ can be expressed as $\lambda_i\left[\mathscr{L}_G \otimes K(\infty)M_\Delta(\infty)\right] = \lambda_i\left[\mathscr{L}_G\right]|k_i(\infty)||m_i(\infty)[1+\delta_i(\infty)]|\angle\left(\phi_i(\infty)+\psi_i(\infty)+\nu_i(\infty)\right)\ \forall i \in \{1,2,\ldots,Nm\}$. Since the eigenvalues of $K(\infty)M_\Delta(\infty)$ are always real numbers (positive/negative/zero) and $K(s)M_\Delta(s)$ does not contain any poles at $s=0$ for any $\delta \in \mathbf{U}$, $\rho_i(+j\infty)$ and $\rho_i(-j\infty)$ coincide and lie either at the origin or on the positive/negative real axis at finite distances from the origin.

Combining Part I and Part II, we can conclude that there always exists a finite range of $\sigma \in (0, \sigma^\star]$ such that none of the characteristic loci $\rho_i(j\omega)$ encircles the worst-case critical point $(-\frac{1}{\sigma^\star}+j0)$ for any uncertainty $\delta(s) \in \mathbf{U}$. This is graphically interpreted through Fig. 15a, which shows that all $\rho_i(s)$ remain inside the Cyan-coloured region for all $\delta(s) \in \mathbf{U}$. Hence, asymptotic stability of the formation control scheme is ensured via Theorem 1 even in the presence of the class of the IM-type uncertainties $\delta \in \mathbf{U}$. After this, it remains to be shown that the formation tracking error decays to zero – which readily follows from [34, Theorem 1] and [44], as mentioned also in the proof of Theorem 2.

The above proof can be easily specialised to the cases where $M(s)$ is SNI. Now, the proof is fully done. ■

Remark 3 *Although Theorem 3 has been derived for* $\mathbf{U}$*-type uncertainties in an input-multiplicative (IM) configuration, it can be readily established the scheme (Fig. 14) can also accommodate the cases when* $\delta(s) \in \mathbf{U}$ *appears in the output-multiplicative or additive form. The same lines of proof of Theorem 3 remain applicable with little modifications and re-adjustments.*

Remark 4 *In contrast to the Lyapunov stability approach used in most MAS-based formation control schemes, the proposed methodology relies on the eigenvalue loci technique to prove the asymptotic convergence of the consensus-tracking error. The proposed scheme i) reduces mathematical complexity, offering a straightforward implementation, ii) removes the need to search for an appropriate Lyapunov function, iii) removes some of the overly restrictive assumptions on the dynamics of the underlying systems and the communication graph to satisfy the formation feasibility condition and iv) does not involve any nonlinear terms in the distributed control law that result in discontinuous control action accompanied by chattering problems. The proposed scheme also exhibits robustness to a class of stable (including NI and PR-type) uncertainties when appearing in a multiplicative/additive form and fault tolerance to a sudden loss of agents.*

6.2 Fault tolerance to a sudden loss of agents

This subsection examines the fault tolerance property of the proposed formation control scheme in the event of a sudden loss of agents due to hardware or communication failures. Exploiting the notion of decentralised integral controllability of NI/SNI systems [4] and inspired by a similar development in the case of single integrator MASs in [12], we will now show that how the overall closed-loop stability can be maintained when some of the agents go out of the network. During the controller design, the effect of the loss of an agent can be considered by making the gain of that particular control loop zero (i.e. $\sigma_i = 0$), which implies that the faulty loop is temporarily deactivated (i.e. the defective agent is excluded from the network). This is done autonomously by the decision-making unit in situations when i) an agent does not communicate with its neighbours continuously for a few seconds (decided w.r.t. the speed of the network), and ii) an agent sends an alarm signal to indicate a hardware failure. In the second case, the inner-loop SMC block helps the faulty UAV to descend and land safely. After the faulty agents are excluded from the network, the decision-making unit executes an autonomous reconfiguration, taking the healthy and active agents. Therefore, a new Laplacian matrix with a reduced dimension is formed, and the distributed 'mixed' SNI+SPR output feedback control law, proposed in (37), drives the agents to achieve a new formation surrounding the leader/target/virtual target and keep tracking the same. The following proposition gives the problem formulation and offers the theoretical proof.

Proposition 1 *Under the assumptions and conditions of Theorem 3, the formation control scheme given in Fig. 14 retains the closed-loop asymptotic stability in the event of a sudden loss of agents under the action of the following distributed 'mixed' SNI+SPR output feedback*

control law

$$\boldsymbol{u}_i = \sigma_i K(s) \sum_{j=1}^{N} a_{ij}\big((\boldsymbol{y}_j - \boldsymbol{h}_j) - (\boldsymbol{y}_i - \boldsymbol{h}_i)\big) + g_i(\boldsymbol{r} + \boldsymbol{h}_i - \boldsymbol{y}_i) \quad \forall i \in \{1, 2, \ldots, N\}. \tag{37}$$

In such cases, after an autonomous reconfiguration of the network, the remaining active agents attain a new formation and keep tracking the target by the designed control law (37).

Proof. The proof essentially builds on Theorem 3 and Theorem 2. The notations and symbols used in this proof are already introduced. Note the slight modification in the control law in (37) compared to (35). Separate controller gains σ_i for $i \in \{1, 2, \ldots, N\}$ are used instead of a common σ. Let $\sigma_i \in [0, \sigma_i^\star]$ and $\sigma^\star = \max\{\sigma_1^\star, \sigma_2^\star, \cdots, \sigma_N^\star\}$.

Theorem 3 can be readily applied to establish the asymptotic stability of the negative feedback formation control scheme given in Fig. 14 for any $\sigma_i \in (0, \sigma^\star]$. We will now show that the closed-loop stability is preserved even when $\sigma_i = 0$ for some $i \in \{1, 2, \ldots, N\}$. This is equivalent to fulfilling the requirement that none of the eigenvalue loci $\rho_i(j\omega)$ of $\big[\mathscr{L}_G \otimes K(s) M_\Delta(s)\big]$ encircles the critical point $(-\frac{1}{\sigma_i} + j0)$ for any $\sigma_i \in [0, \sigma^\star]$, particularly when $\sigma_i = 0$ for some i. Fig. 15b portrays the locus of the critical points starting from $(-\frac{1}{\sigma^\star} + j0)$ up to $(-\infty + j0)$ when σ_i varies in the range $[0, \sigma^\star]$. Note that the critical point $(-\frac{1}{\sigma_i} + j0)$ reaches $(-\infty + j0)$ when $\sigma_i = 0$, which corresponds to a faulty situation of the i^{th} agent. Fig. 15b nicely depicts that the full set of the critical points $(-\frac{1}{\sigma_i} + j0)$ for $\sigma_i \in [0, \sigma^\star]$ remains outside the Pink-coloured region in Fig. 15b. This, hence ensures that even though the i^{th} critical point lies at $(-\infty + j0)$, it will not be encircled by the eigenvalue loci $\rho_i(j\omega)$.

Under a faulty situation, the decision-making unit overwrites the σ_i values (of the faulty agents) to zero, which indicates that the faulty agents have been excluded from the network without impairing the stability of the overall network. The inner-loop controller will then help the faulty UAV safely reach the ground. In the meantime, the decision-making unit will also initiate an autonomous network reconfiguration, taking the healthy/active agents. This will give rise to a new topology with fewer agents. However, the bidirectional communication topology will be maintained. Hence, the new Laplacian matrix will retain the same properties as before. Finally, the agents will achieve a formation surrounding the given target/leader by the same distributed control law (37) following the same principle derived in Theorem 3 and keep tracking the target. This completes the proof. ■

7 Case study and Matlab simulation results

This section presents the formation control design for a network of six multi-tilt tricopter agents using the results developed in Section 5. These six agents have identical NI dynamics based on the inner-loop-SMC-controlled model identified in Subsection 4.2. MATLAB simulation results are presented to show the effectiveness of the proposed scheme.

7.1 Formation control of a group of multi-tilt tricopters in the ideal case

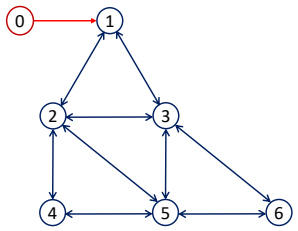

Fig. 16. A bidirected interaction topology.

For this case study, we consider a group of six multi-tilt tricopter UAVs, and the control objective is to achieve a desired formation and escort a leader or target to its destination. Each of the six agents has identical LTI state-space dynamics described by,

$$\dot{x}_i = Ax_i + Bu_i \quad \text{and} \quad y_i = Cx_i \quad \forall i \in \{1, 2, \ldots, 6\},$$

where $x_i = \begin{bmatrix} \dot{x}_i & x_i & \dot{y}_i & y_i & \dot{z}_i & z_i & \dot{\phi}_i & \phi_i & \dot{\theta}_i & \theta_i & \dot{\psi}_i & \psi_i \end{bmatrix}^\top$, $u_i = \begin{bmatrix} x_{di} & y_{di} & z_{di} & \phi_{di} & \theta_{di} & \psi_{di} \end{bmatrix}^\top$, $y_i = \begin{bmatrix} x_i & y_i & z_i & \phi_i & \theta_i & \psi_i \end{bmatrix}^\top$ and the matrices A, B, C are given as

$$A = \begin{bmatrix} -63 & -56 & 0 & 0 & 0 & 0 & 0 & 0 & 0 & 0 & 0 & 0 \\ 78 & 0 & 0 & 0 & 0 & 0 & 0 & 0 & 0 & 0 & 0 & 0 \\ 0 & 0 & -66 & -47 & 0 & 0 & 0 & 0 & 0 & 0 & 0 & 0 \\ 0 & 0 & 78 & 0 & 0 & 0 & 0 & 0 & 0 & 0 & 0 & 0 \\ 0 & 0 & 0 & 0 & -64 & -39 & 0 & 0 & 0 & 0 & 0 & 0 \\ 0 & 0 & 0 & 0 & 78 & 0 & 0 & 0 & 0 & 0 & 0 & 0 \\ 0 & 0 & 0 & 0 & 0 & 0 & -123 & -67 & 0 & 0 & 0 & 0 \\ 0 & 0 & 0 & 0 & 0 & 0 & 78 & 0 & 0 & 0 & 0 & 0 \\ 0 & 0 & 0 & 0 & 0 & 0 & 0 & 0 & -136 & -75 & 0 & 0 \\ 0 & 0 & 0 & 0 & 0 & 0 & 0 & 0 & 78 & 0 & 0 & 0 \\ 0 & 0 & 0 & 0 & 0 & 0 & 0 & 0 & 0 & 0 & -32 & -85 \\ 0 & 0 & 0 & 0 & 0 & 0 & 0 & 0 & 0 & 0 & 156 & 0 \end{bmatrix} \times 10^{-4},$$

$$B = \begin{bmatrix} 625 & 0 & 0 & 0 & 0 & 0 \\ 0 & 0 & 0 & 0 & 0 & 0 \\ 0 & 625 & 0 & 0 & 0 & 0 \\ 0 & 0 & 0 & 0 & 0 & 0 \\ 0 & 0 & 625 & 0 & 0 & 0 \\ 0 & 0 & 0 & 0 & 0 & 0 \\ 0 & 0 & 0 & 625 & 0 & 0 \\ 0 & 0 & 0 & 0 & 0 & 0 \\ 0 & 0 & 0 & 0 & 625 & 0 \\ 0 & 0 & 0 & 0 & 0 & 0 \\ 0 & 0 & 0 & 0 & 0 & 1250 \end{bmatrix} \times 10^{-4} \text{ and}$$

$$C = \begin{bmatrix} 4 & 720 & 0 & 0 & 0 & 0 & 0 & 0 & 0 & 0 & 0 & 0 \\ 0 & 0 & 0 & 556 & 0 & 0 & 0 & 0 & 0 & 0 & 0 & 0 \\ 0 & 0 & 0 & 0 & 0 & 487 & 0 & 0 & 0 & 0 & 0 & 0 \\ 0 & 0 & 0 & 0 & 0 & 0 & 0 & 989 & 0 & 0 & 0 & 0 \\ 0 & 0 & 0 & 0 & 0 & 0 & 0 & 0 & 0 & 1162 & 0 & 0 \\ 0 & 0 & 0 & 0 & 0 & 0 & 0 & 0 & 0 & 0 & 0 & 763 \end{bmatrix} \times 10^{-4}.$$

The above model represents the inner-loop-SMC-controlled multi-tilt tricopter system $M(s) = \text{diag}\{m_j(s)\} \in$

$\mathscr{RH}_\infty^{6\times 6}$ $\forall j \in \{1, 2, \ldots, 6\}$ using (28)–(33), with m inputs and outputs, which was identified in Subsection 4.2, and satisfies the NI property. It can also be easily verified that (A, B, C) is stabilizable and detectable. The undirected interaction topology among the six vehicles is given in Fig. 16, where the leader agent or target (labelled '0') provides the formation reference signal. It follows from Fig. 16 that the Laplacian of the network is

$$\mathscr{L} = \begin{bmatrix} 2 & -1 & -1 & 0 & 0 & 0 \\ -1 & 4 & -1 & -1 & -1 & 0 \\ -1 & -1 & 4 & 0 & -1 & -1 \\ 0 & -1 & 0 & 2 & -1 & 0 \\ 0 & -1 & -1 & -1 & 4 & -1 \\ 0 & 0 & -1 & 0 & -1 & 2 \end{bmatrix}, \tag{38}$$

and since only the first agent is connected to the leader, an edge $(0, 1)$ exists between them with a pinning gain $g_1 = 1$ while $g_i = 0$ for $i \in \{2, \ldots, 6\}$.

We choose a high-gain SNI controller $k_1(s) = \frac{10^7}{(s+\rho_1)}$ to stabilize the x position and a set of high-gain SPR controllers of the form $k_j(s) = \frac{8\times 10^7 (s+2)}{(s+\rho_j)}$ $\forall j \in \{2, 3, \ldots, 6\}$ for the rest of the channels with $\rho = \begin{bmatrix}\rho_1, \rho_2, \ldots, \rho_6\end{bmatrix} = \begin{bmatrix}15, 100, 80, 90, 95, 49\end{bmatrix}$. Consequently, the 'mixed' SNI+SPR controller is given as $K(s) = \text{diag}\{k_j\}$ $\forall j \in \{1, 2, \ldots, 6\}$ with $\sigma = 1$, and it is trivial to show that $K(0) > 0$ as required. As depicted in Fig. 13, the group formation reference which achieves the desired formation is given as $(\mathbf{r} + \mathbf{h}) \in \mathbb{R}^{36}$ where $\bar{\mathbf{r}} = \begin{bmatrix}\boldsymbol{r}^\top \ \boldsymbol{r}^\top, \ldots, \boldsymbol{r}^\top\end{bmatrix}^\top \in \mathbb{R}^{36}$ is the formation reference and $\mathbf{h} = \begin{bmatrix}\boldsymbol{h}_1^\top \ \boldsymbol{h}_2^\top, \ldots, \boldsymbol{h}_6^\top\end{bmatrix}^\top \in \mathbb{R}^{36}$ is the formation configuration. The reference for the leader or root node is selected as $\mathbf{r}_0 = \begin{bmatrix}4 \ 3 \ 2 \ 0 \ 0 \ 0\end{bmatrix}^\top$ $\forall t < 10$s and $\mathbf{r}_0 = \begin{bmatrix}-1 \ 5 \ 3.2 \ 0 \ 0 \ 0\end{bmatrix}^\top$ $\forall t \geq 10$s.

The formation configuration for the followers was chosen as

$$\boldsymbol{h}_i = \begin{bmatrix} \gamma \cos\left(\frac{(i+1)\pi}{3}\right) \\ \gamma \sin\left(\frac{(i+1)\pi}{3}\right) \\ 0 \\ \gamma \sin\left(\frac{(i+1)\pi}{3}\right) \\ \gamma \cos\left(\frac{(i+1)\pi}{3}\right) \\ 0 \end{bmatrix} \quad \forall t < 10\text{s}$$

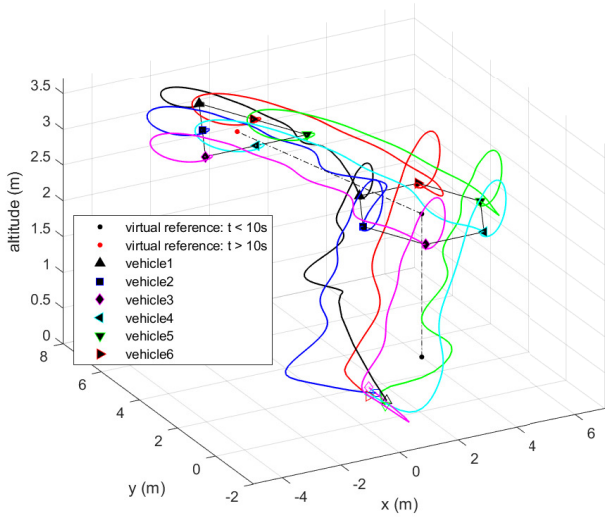

Fig. 17. Group formation of six tricopter agents with SNI+SPR controllers with formation configuration switched from diamond to triangle after 10 seconds.

and

$$\boldsymbol{h}_i = \begin{bmatrix} \beta_i \cos\left(\frac{(2i+1)\pi}{6}\right) \\ \beta_i \sin\left(\frac{(2i+1)\pi}{6}\right) \\ 0 \\ 0 \\ 0 \\ 0 \end{bmatrix} \quad \forall t \geq 10\text{s}$$

$\forall i \in \{1, 2, \ldots, 6\}$ where $\gamma = 2.0$ m is the radius of the formation, $\beta_i = \gamma$ $\forall i \in \{1, 3, 5\}$ and $\beta_i = \gamma/2$ $\forall i \in \{2, 4, 6\}$. Initially, with $t < 10s$, the follower agents track a diamond formation bordering the leader agent, while for $t \geq 10$s, the follower agents track a triangle formation with respect to the formation configuration $\boldsymbol{h}_i$, taking into account a change in the leader reference $\mathbf{r}$ at $t = 10$s. Fig. 17 shows that the six multi-tilt tricopter agents achieve leader-following consensus and formation tracking as $t \to \infty$. Note that if $\mathbf{h} = 0$, the entire scheme in Fig. 13 reduces to a consensus problem. It, therefore, follows that the SNI+SPR controller inherently achieves consensus tracking. When the leader reference and demanded group formation changes at $t = 10$s, the SNI+SPR control scheme maintains the stability of the entire network. It ensures that the six multi-tilt tricopter agents track the newly demanded triangle formation.

Figures 18–20 show the responses of the positions x_i, y_i, z_i $\forall i \in \{1, 2, \ldots, 6\}$ to the demanded references. For the six follower agents, the actual positions track the demanded leader within 5 seconds before and after the period $t \geq 0$, corresponding to a change in the demanded group formation. Similarly, Figures 21–23 show

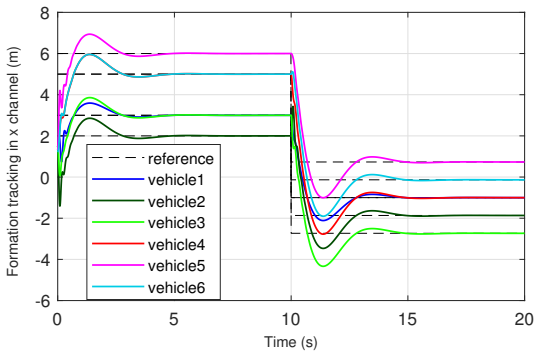

Fig. 18. x position responses.

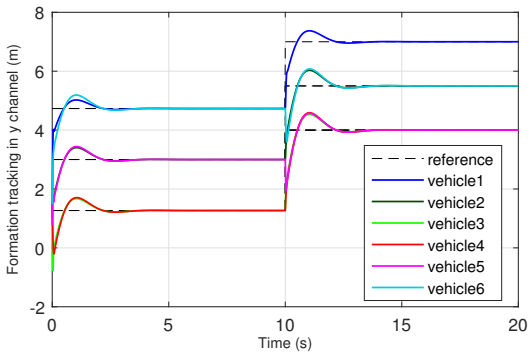

Fig. 19. y position responses.

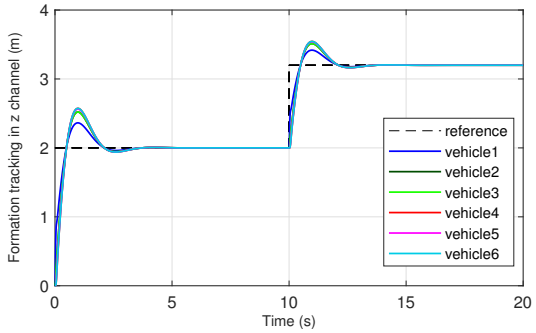

Fig. 20. altitude z responses.

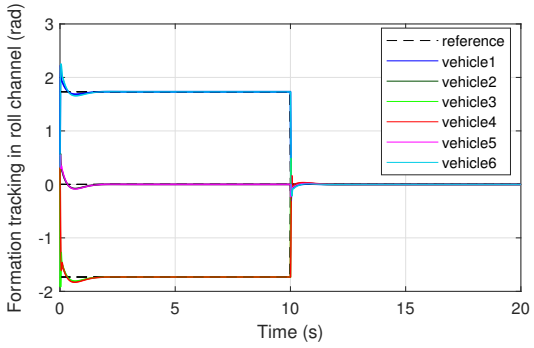

Fig. 21. roll attitude responses.

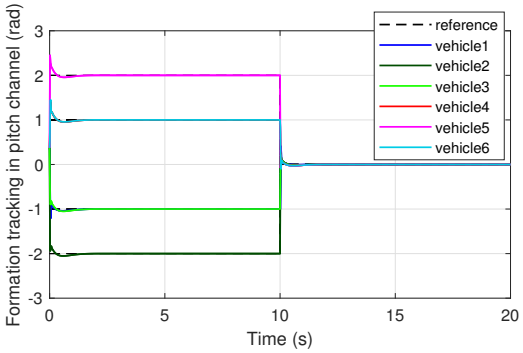

Fig. 22. Pitch attitude responses.

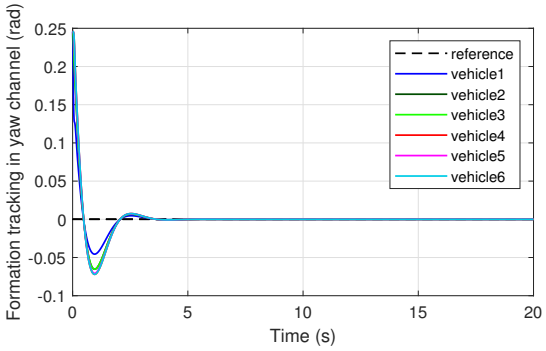

Fig. 23. Yaw attitude responses.

that the attitudes of the six multi-tilt tricopter agents track the target attitude. Considering Figures 21–23, it is also worth noting that for $t < 10$s, the motion of the multi-tilt tricopter agents occurs with a change in attitude, implying simultaneous position and attitude control, which is an advantage of the tricopter under consideration due to its airframe configuration. For $t > 10$s, the case where the tricopter agents translate to track the leader or target without a change in attitude is evident, indicating the ability of the tricopter under consideration to achieve simultaneous independent attitude and trajectory control, extending the limits of the classic tricopter [1] and other commonly used multirotor UAVs such as quadcopters.

7.2 Formation control of a group of multi-tilt tricopters with Uncertainty

The same team of six multi-tilt tricopters is simulated following the scheme in Fig. 14, considering an IM-type uncertainty $\delta_i = \frac{1}{s^2+s+1}$ $\forall i \in \{1, 2, \ldots, 6\}$ in each of the six axes. We denote $\Delta_i = \text{diag}\{\delta_i\}$ and $\overline{\Delta} = \text{diag}\{\Delta_i\}$. Fig. 24 reveals that the NI-based cooperative control scheme has satisfactorily achieved formation control for all six agents, even in the presence of uncertainties. Although there is a performance degradation, still, it can be regarded as the robustness of the proposed scheme. We also tested the near-worst-case scenario by considering uncertainties in all six axes of the multi-tilt tricopter.

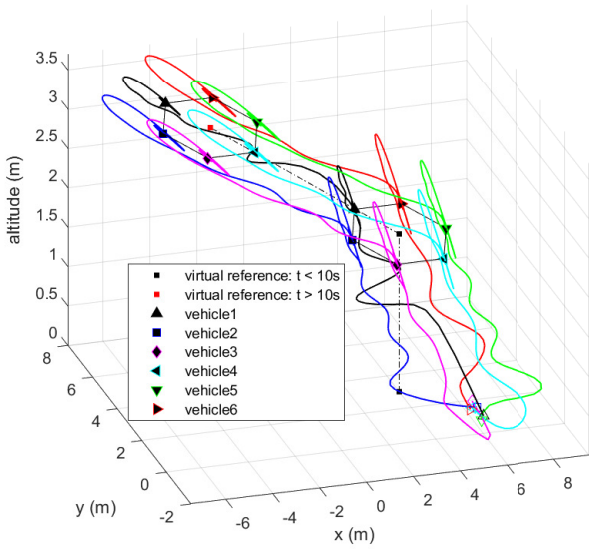

Fig. 24. Formation control achieved in the presence of IM–type uncertainty in each axis of the multi-tilt tricopter UAVs.

7.3 Formation control of a group of multi-tilt tricopters with faulty agents

To show the fault tolerance properties of the proposed scheme, we use the control law in (37) where the integral gain $\sigma_i = 1$ for $i = \{1, 2, 3, 5, 6\}$ and $\sigma_4 = 0$ indicating a fault in vehicle 4. The fault is introduced after 10 seconds, and the proposed scheme can deactivate the faulty vehicle within a short period and reconfigure the network to use only the remaining five agents to achieve an alternative formation as in Fig. 25.

8 Conclusion

This paper has exploited 'a blend of NI and PR theory' to design a robust formation control scheme for a group of multi-tilt tricopter agents. We have also developed a closed-loop system identification technique in the continuous time domain and imposed NI constraints to obtain an NI model. First, we derived a complete nonlinear kinematic and dynamic model of a multi-tilt tricopter. A sliding mode control (SMC) scheme was designed to achieve stable hovering. The identification algorithm was then run on the SMC-controlled tricopter hovering at a certain height, and a second-order NI model was identified in the closed loop for each of the six channels $(x, y, z, \phi, \theta, \psi)$. After that, a distributed output feedback formation control scheme was developed for a group of SMC-controlled tricopter agents (whose closed-loop dynamics satisfy the NI property) exploiting a 'mixed' SNI+SPR control law. This two-loop control strategy

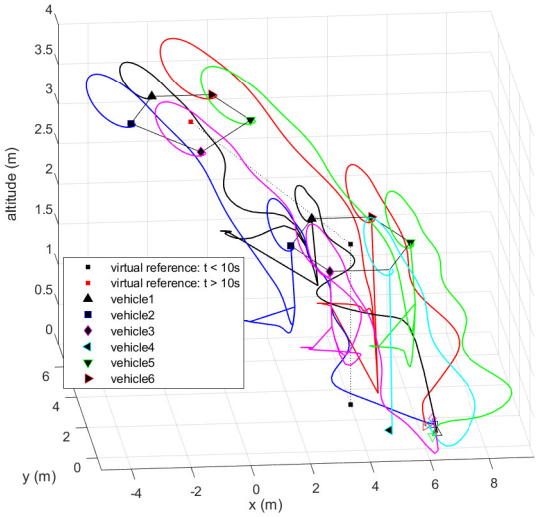

Fig. 25. Multi-tilt tricopter agents with a fault on vehicle 4

helps to achieve the target position and attitude of the tricopters, independent of each other. The theoretical proof relies on the characteristic loci technique instead of the Lyapunov stability approach commonly used in the cooperative control literature. MATLAB simulation results showed decent performance and robustness to NI-type uncertainties. Group formation control problems and obstacle avoidance aspects can be considered in the future.

Acknowledgements

We would like to sincerely thank the anonymous reviewers and Associate Editor for giving their constructive feedback, valuable guidelines and suggestions that helped enrich the paper's technical contributions.

References

[1] D. Abara, S. Kannan, and A. Lanzon. Development and stabilization of a low-cost single-tilt tricopter. *IFAC-PapersOnLine*, 53(2):8897–8902, July 2020. 21st IFAC World Congress, Berlin, Germany.

[2] J. J. Belletrutti and A. G. J. MacFarlane. Characteristic loci techniques in multivariable-control-system design. *Proceedings of the Institution of Electrical Engineers*, 118(9):1291–1297, Sep 1971.

[3] B. Bhikkaji, S. O. Reza Moheimani, and I. R. Petersen. A negative imaginary approach to modeling and control of a collocated structure. *IEEE/ASME Transactions on Mechatronics*, 17(4):717–727, Aug 2012.

[4] P. Bhowmick and S. Patra. On decentralized integral controllability of stable negative-imaginary systems and some related extensions. *Automatica*, 94:443–451, 2018.

[5] C. Cai and G. Hagen. Stability analysis for a string of coupled stable subsystems with negative imaginary frequency response. *IEEE Transactions on Automatic Control*, 55(8):1958–1963, Aug 2010.

[6] P. Castillo, A. Dzul, and R. Lozano. Real-time stabilization and tracking of a four-rotor mini rotorcraft. *IEEE Transactions on Control Systems Technology*, 12(4):510–516, 2004.

[7] S. K. Das, H. R. Pota, and I. R. Petersen. Stability analysis for interconnected systems with "mixed" passivity, negative-imaginary and small-gain properties. In *Proceedings of Australian Control Conference*, pages 201–206, Nov 2013.

[8] B. R. J. Haverkamp, C. T. Chou, M. H. Verhaegen, and R. Johansson. Identification of continuous-time MIMO state space models from sampled data, in the presence of process and measurement noise. In *Proceedings of the 35th IEEE Conference on Decision and Control*, pages 1539–1544, Kobe, Japan, Dec 1996. IEEE.

[9] B. R. J. Haverkamp, M. Verhaegen, C. T. Chou, and R. Johansson. Continuous-time subspace model identification method using laguerre filtering. *IFAC Proceedings Volumes*, 30(11):1093–1098, July 1997.

[10] J. Hu, P. Bhowmick, and A. Lanzon. Distributed adaptive time-varying group formation tracking for multi-agent systems with multiple leaders on directed graphs. *IEEE Transactions on Control of Network Systems*, 7(1):140–150, 2020.

[11] J. Hu and A. Lanzon. An innovative tri-rotor drone and associated distributed aerial drone swarm control. *Robotics and Autonomous Systems*, 103:162–174, May 2018.

[12] J. Hu, B. Lennox, and F. Arvin. Robust formation control for networked robotic systems using negative imaginary dynamics. *Automatica*, 140(C), Jun 2022.

[13] M. Kara-Mohamed and A. Lanzon. Design and control of novel tri-rotor UAV. In *Proceedings of UKACC International Conference on Control*, pages 304–309, Cardiff, UK, September 2012.

[14] H. K. Khalil. *Nonlinear Systems*. Prentice-Hall, Englewood Cliffs, NJ, 2nd edition, 1996.

[15] J. Kim, M-S. Kang, and S. Park. Accurate modeling and robust hovering control for a quad-rotor VTOL aircraft. *Journal of Intelligent and Robotic Systems*, 57, 2010.

[16] A. Lanzon and H-J. Chen. Feedback stability of negative imaginary systems. *IEEE Transactions on Automatic Control*, 62(11):5620–5633, Nov 2017.

[17] A. Lanzon, A. Freddi, and S. Longhi. Flight control of a quadrotor vehicle subsequent to a rotor failure. *AIAA Journal of Guidance, Control and Dynamics*, 37(2):580–591, 2014.

[18] A. Lanzon and I. R. Petersen. Stability robustness of a feedback interconnection of systems with negative imaginary frequency response. *IEEE Transactions on Automatic Control*, 53(4):1042–1046, May 2008.

[19] C. Li, J. Wang, J. Shan, A. Lanzon, and I. R. Petersen. Robust cooperative control of networked train platoons: A negative-imaginary systems' perspective. *IEEE Transactions on Control of Network Systems*, 8(4):1743–1753, Dec 2021.

[20] M. Liu, J. Lam, H. Lin, and X. Jing. Necessary and sufficient conditions on negative imaginariness for interval SISO transfer functions and their interconnection. *IEEE Transactions on Automatic Control*, 65(10):4362–4368, 2020.

[21] L. Ljung. *System Identification: Theory for the User*. Prentice Hall information and system sciences series. Prentice Hall, 1999.

[22] M. A. Mabrok, M. A. Haggag, I. R. Petersen, and A. Lanzon. A subspace system identification algorithm guaranteeing the negative imaginary property. In *Proceedings of the 53rd IEEE Conference on Decision and Control*, pages 3180–3185, Los Angeles, CA, USA, December 2014.

[23] M. A. Mabrok, A. G. Kallapur, I. R. Petersen, and A. Lanzon. Generalizing negative imaginary systems theory to include free body dynamics: Control of highly resonant structures with free body motion. *IEEE Transactions on Automatic Control*, 59(10):2692–2707, Oct 2014.

[24] A. G. J. Macfarlane and J. J. Belletrutti. The characteristic locus design method. *Automatica*, 9(5):575–588, 1973.

[25] R. Mahony, V. Kumar, and P. Corke. Multirotor aerial vehicles: Modeling, estimation, and control of quadrotor. *IEEE Robotics Automation Magazine*, 19(3):20–32, 2012.

[26] R. Mohd-Mokhtar and L. Wang. Continuous time state space model identification using closed-loop data. In *2008 Second Asia International Conference on Modelling Simulation (AMS)*, pages 812–817, 2008.

[27] T. P. Nascimento and M. Saska. Position and attitude control of multi-rotor aerial vechcles: A survey. *Annual Reviews in Control*, 48:129–146, 2019.

[28] N. Nikooienejad and S. O. Reza Moheimani. Convex synthesis of SNI controllers based on frequency-domain data: MEMS nanopositioner example. *IEEE Transactions on Control Systems Technology*, 30(2):767–778, March 2022.

[29] G. D. Padfield. *Helicopter Flight Dynamics: The Theory and Application of Flying Qualities and Simulation Modeling*. Blackwell Publishing, Oxford, UK, 2nd edition, 1996.

[30] S. Patra and A. Lanzon. Stability analysis of interconnected systems with "mixed" negative-imaginary and small-gain properties. *IEEE Transactions on Automatic Control*, 56(6):1395–1400, June 2011.

[31] A. Prach and E. Kayacan. An MPC-based position controller for a tilt-rotor tricopter VTOL UAV. *Optimal control applications and methods*, 39(1):343–356, 2018.

[32] R. W. Prouty. *Helicopter Performance, Stability*

and Control. Krieger Publishing Company, Malabar, Florida, 1995.

[33] M. Senanayake, I. Senthooran, J. C. Barca, H. Chung, J. Kamruzzaman, and M. Murshed. Search and tracking algorithms for swarms of robots: A survey. *Robotics and Autonomous Systems*, 75:422–434, 2016.

[34] J. H. Seo, H. Shim, and J. Back. Consensus of high-order linear systems using dynamic output feedback compensator: Low gain approach. *Automatica*, 45(11):2659–2664, 2009.

[35] A. Shukla and H. Karki. Application of robotics in onshore oil and gas industry—a review part i. *Robotics and Autonomous Systems*, 75:490–507, 2016.

[36] O. Skeik, J. Hu, F. Arvin, and A. Lanzon. Cooperative control of integrator negative imaginary systems with application to rendezvous multiple mobile robots. In *Proceedings of the 12th International Workshop on Robot Motion and Control*, pages 15–20, Poznan, Poland, July 2019. IEEE.

[37] B. L. Stevens, F. L. Lewis, and E. N. Johnson. *Aircraft Control and Simulation: Dynamics, Controls Design, and Autonomous Systems*. John Wiley and Sons, Hoboken, New Jersey, 2015.

[38] V. P. Tran, M. A. Garratt, and I. R. Petersen. Switching time-invariant formation control of a collaborative multi-agent system using negative imaginary systems theory. *Control Engineering Practice*, 95(104245):1–16, Nov 2020.

[39] V. P. Tran, M. A. Garratt, and I. R. Petersen. Multi-vehicle formation control and obstacle avoidance using negative-imaginary systems theory. *IFAC Journal of Systems and Control*, 15:1–23, March 2021.

[40] M. H. Trinh, S. Zhao, Z. Sun, D. Zelazo, B. D. O. Anderson, and H-S. Ahn. Bearing-based formation control of a group of agents with leader-first follower structure. *IEEE Transactions on Automatic Control*, 64(2):598–613, 2019.

[41] P. van Overschee and B. L. de Moor. *Subspace Identification for Linear Systems: Theory, Implementation, Applications.* Springer, Boston, MA, 1st edition, 1996.

[42] C. Wang, H. Tnunay, Z. Zuo, B. Lennox, and Z. Ding. Fixed-time formation control of multirobot systems: Design and experiments. *IEEE Transactions on Industrial Electronics*, 66(8):6292–6301, 2019.

[43] J. Wang, A. Lanzon, and I. R. Petersen. Robust cooperative control of multiple heterogeneous negative-imaginary systems. *Automatica*, 61:64–72, 2015.

[44] J. Wang, A. Lanzon, and I. R. Petersen. Robust output feedback consensus for networked negative-imaginary systems. *IEEE Transactions on Automatic Control*, 60(9):2547–2552, Sep. 2015.

[45] J. Xiong, I. R. Petersen, and A. Lanzon. A negative imaginary lemma and the stability of interconnections of linear negative imaginary systems. *IEEE Transactions on Automatic Control*, 55(10):2342–2347, Oct 2010.